Exploring two-phase hydrothermal circulation at a seafloor pressure of 25 MPa: Application for EPR 9°50' N

Liang Han

Thesis submitted to the faculty of the Virginia Polytechnic Institute and State University in partial fulfillment of the requirements for the degree of

Master of Science

In

Geosciences

Robert P. Lowell

Robert J. Bodnar

John A. Hole

Scott D. King

October 21, 2011

Blacksburg, VA

Keywords: seafloor hydrothermal system, FISHES, two phase flow, numerical modeling, East Pacific Rise, H_2O-NaCl

Exploring two-phase hydrothermal circulation at a surface pressure of 25 MPa: Application for EPR 9°50' N

Liang Han

ABSTRACT

We present 2-D numerical simulations of two phase flow in seafloor hydrothermal systems using the finite control volume numerical scheme FISHES. The FISHES code solves the coupled non-linear equations for mass, momentum, energy, and salt conservation in a NaCl-H_2O fluid to model the seafloor hydrothermal processes. These simulations use homogeneous box geometries at a fixed seafloor pressure of 25 MPa with constant bottom temperature boundary conditions that represent a sub-axial magma chamber to explore the effects of permeability, maximum bottom temperature and system depth on the evolution of vent fluid temperature and salinity, and heat output. We also study the temporal and spatial variability in hydrothermal circulation. The two-phase simulation results show that permeability plays an important role in plume structure and heat output of hydrothermal systems, but it has little effect on vent fluid temperature and salinity, given the same bottom temperature. For some permeability values, multiple plumes can vent at the seafloor above the simulated magma chamber. Temporal variability of vent fluid temperature and salinity and the complexity of phase separation suggest that pressure and temperature conditions at the top of the axial magma chamber cannot be easily inferred from vent fluid temperature and salinity alone. Vapor and brine derived fluids can vent at the seafloor simultaneously, even from neighboring locations that are fed by the same plume.

To Chengyun Li, my dear family, friends and teachers.

ACKNOWLEDGEMENTS

First of all, I would like to express my sincere thanks to my advisor Dr. Robert. P. Lowell, who introduced me to USA and offered me the opportunity to pursue my M.S. and Ph.D. degree. He has been my teacher and friend during my M.S. program, and he will still be my co-advisor for my Ph. D program. There is an old Chinese adage "Once a teacher, forever a teacher like father." Please accept a Chinese formal greeting. He teaches me English and personality, and leaded me to the geophysics world. He is always open to talk with not only on the problems in the research, but also the troubles in personal life. I appreciate his countless guidance, support, encouragement and endurance in my academic pursuits. I also appreciate his understanding, enlightenment, respect and support when I was depressed or made a different choice. What I have got from him is not limited to geophysics or science, but rather is applicable to my entire life.

I would like to thank my committee members: Dr. Robert Bodnar, Dr. Scott King and Dr. John Hole for providing me helpful suggestions on my research and my M.S. Thesis. Dr. Bodnar is always open to students and patient to lead them to the truth. I have often received help from his lectures and personal discussions, particularly about NaCl-H_2O phase diagram, magma system and other geochemical knowledge. Dr. King is an expert on numerical modeling, whose strict and critical suggestions and concerns make me evaluate and interpret my work much more carefully. Dr. Hole will also be my advisor for my Ph. D. program. I appreciate his understanding and support for my M.S. Thesis defense, and I enjoyed the conversation with him on seismology and tectonics. Although Dr. Ying Zhou, Dr. Chester Weiss, Dr. Martin Chapman

and Dr. Robert Tracy are not on the list of my committee members, I would like to thank them for what I have learned in their classes.

My earnest thanks also go to my group members, Kayla Lewis, Kate Craft, Lei Liu, Matt Steele-Maclnnis, Aida Farough, Shreya Singh, Jaewoon Choi, Dave Mercier and Iliya Smithka, for the insightful discussion and generous help along the way. I also would like to thank my other friends at Virginia Tech, Kui Liu, Youyi Ruan and his wife Wei Sun, Changyeol Lee, Di Wang, Meijing Zhang, Kai Wang, Nizhou Han, Oluyinka Oyewumi, Daniel Moncada, Rosario Esposito, Pilar Lecumberri Sanchez, Carol Johnson, Kathy Davenport, Samuel Fortson, Pavithra Sekhar, Eric Kazlaukas, Karina Cheung, Ariel Conn, Tannistha Maiti, Sharmin Shamsalsadati, and Matthew Francis for their friendships. I regret not to enumerate all the friends here.

Last but not least, I would like to express my deepest gratitude to my family. I would like to thank my parents, my sister and my girlfriend for pure, unconditional and eternal love. They have given me the strength and courage to complete this work and move forward in life.

Funding for this work was provided by National Science Foundation, grants OCE-0819084 and OCE-0926418 to Dr. Robert Lowell. This support is gratefully acknowledged.

TABLE OF CONTENTS

LIST OF FIGURES

LIST OF TABLES

CHAPTER 1: INTRODUCTION

1.1 Seafloor hydrothermal systems

Oceanic spreading centers are sites where new oceanic lithosphere is created as part of Earth's dynamic tectonics. They extend ~80,000 km across the seafloor and are sites where vigorous thermal, chemical and biological activity results from hydrothermal circulation. Seafloor hydrothermal circulation transports ~25% of global heat flux from earth interior, and ~33% of oceanic heat flux through seafloor [*Williams and Von Herzen,* 1974; *Sclater et al.,* 1980]. As shown schematically in Figure 1.1, hydrothermal circulation occurs as cold seawater enters the permeable crustal rocks at oceanic spreading centers, is heated as it flows horizontally near the top of axial magma chamber (AMC), and then discharges as hot (~ 350-400°C) metal-

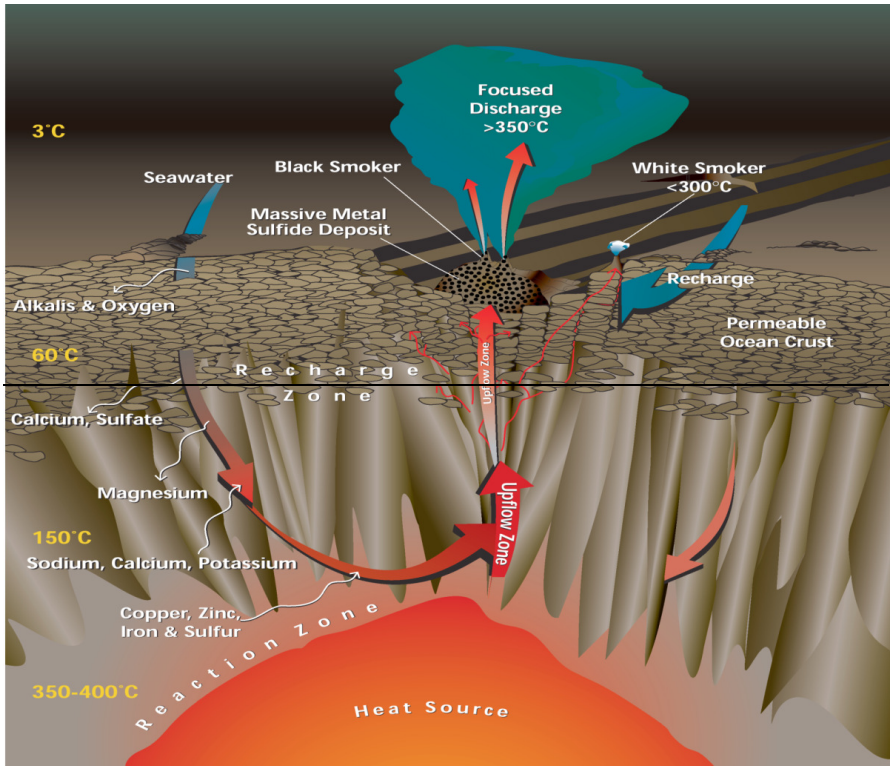

Figure 1.1 A sketch of seafloor hydrothermal system. [www.whoi.edu]

Laden fluid on the seafloor.

During hydrothermal circulation, intense water-rock chemical reactions occur, which give rise to rock alteration and control the chemical composition of the hydrothermal fluids. These reactions affect geochemical cycles of major and trace elements (Mg, S, Ca, Si, Fe, and others) [*Von Damm,* 2004]. Moreover, hydrothermal fluids may create seafloor ore deposits and support both subsurface microbial communities and macrofaunal biological communities on the seafloor. Additional details on hydrothermal systems at oceanic spreading centers can be found in a series of monographs [e.g., *Humphris et al.,* 1995; *Buck et al.,* 1998; *Wilcock et al.,* 2004; *German et al.,* 2004; *Lowell et al.,* 2008; and *Rona et al.*, 2010].

1.2 Vent fluid salinity

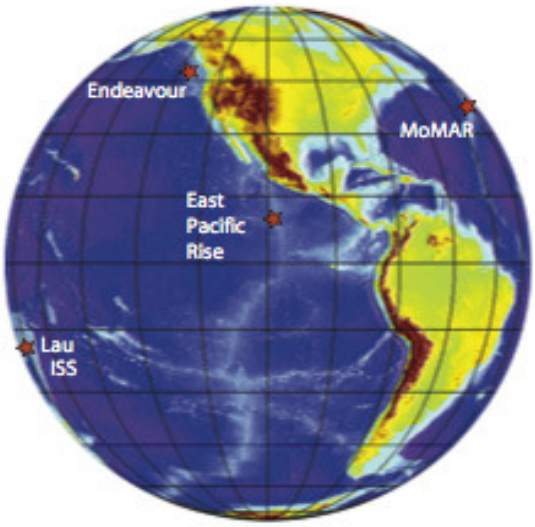

Figure 1.2 Globe map showing the locations of current and planned Integrated Studies Sites. [www.ridge2000.org]

Figure 1.2 shows the globe map with locations of current and planned Integrated Studies Sites, including East Pacific Rise (EPR), Main Endeavour Field (MEF), Mid-Atlantic Ridge

(MAR) and Lau basin. One of the most striking features of those hydrothermal vent fluids is that their salinity differs significantly from seawater (Figure 1.3). Figure 1.3 shows that vent fluid

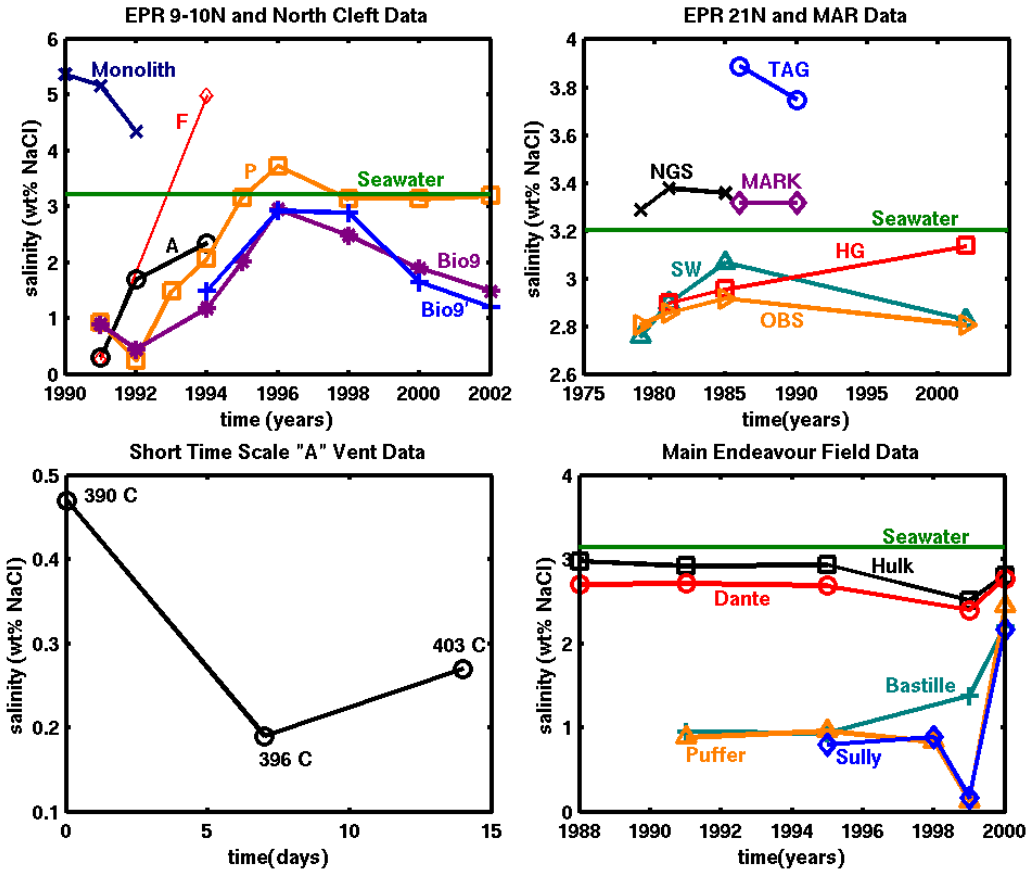

Figure 1.3 Summary of vent fluid salinity data from the literature. In the upper left panel, Monolith is a North Cleft site on the JDF (Juan de Fuca); the others are from EPR 9-10 ˚N. In the upper right panel, TAG and MARK refer to MAR sites; the others refer to EPR at 21˚N. The lower left panel is a two-week time series of vent fluid salinity and temperature at "A" vent at 9˚N EPR. The lower right panel shows sites from the Main Endeavor Vent Field, JDF. Data prior to 1995 are taken from *Von Damm* [1995]. More recent data from 9° N EPR are from *Von Damm* [2004] and those from 21°N EPR are from *Von Damm et al.* [2002]. More recent data from Main Endeavor are from *Lilliey et al.* [2003]. [from *Lewis and Lowell*, 2004].

salinity ranges from an equivalent of about 0.2wt% to about 5.5wt% NaCl, or from less than 10% to approximately 200% of normal seawater salinity, which can be approximated as a 3.2 wt% NaCl-H_2O solution [e.g., *Bischoff and Rosenbauer*, 1984]. As shown in Figure 1.3, more data are available for EPR 9°-10° N and MEF than elsewhere, but the data are still too limited to

provide a clear overview of the entire evolution of vent fluid salinity with time. Figure 1.3 also shows that different vents within the same vent field may exhibit somewhat different salinities while undergoing somewhat similar temporal variations. For example, in the upper left panel of Figure 1.3, the vent fluid salinity at EPR 9°-10° N has evolved in a similar pattern between 1991 and 2002, with a gradual rise in salinity between 1992 and 1996, followed by a decrease. In addition, Bio9 and P vent, which are separated by approximately 60m, have noticeably different salinities, and the vent fluid salinity of P vent was above seawater salinity while that of Bio 9 vent was below seawater salinity in 1996 [*Von Damm*, 2004].

The variations in vent fluid salinity are generally thought to result from phase separation of seawater as it is heated upon entering the two-phase region in P-T-X space. This idea is supported by fluid inclusion study on ophiolites and oceanic crust (e.g., Kelley and Delaney, 1987; Nehlig, 1991). The phase separation process can be better understood by referring to the phase diagram of NaCl-H_2O (Figure 1.4).

As shown in Figure 1.4, the phase diagram is separated into 5 regions, including a vapor + halite (V+H) coexistence region, a vapor + liquid (V+L) coexistence region, and a liquid + halite (L+H) coexistence region on the low temperature and/or low salinity side of halite liquidus surface. Two of the regions contain only a single phase. The liquid (or single phase fluid with liquid-like density) region occurs on the high pressure and/or high salinity side of V+L coexistence region, and the vapor (or single phase fluid with vapor-like density) region occurs on the low pressure and/or lower salinity of V+L coexistence region. The boundary between vapor and liquid for H_2O is defined by a line in PT space, whereas the liquid-vapor coexistence region for NaCl-H_2O is defined by a volume in P-T-X space. The vapor-liquid critical point for H_2O denotes the conditions (pressure and temperature) above which distinct liquid and gas

phases do not exist. The boiling curve for H_2O terminates at the H_2O critical point (373.976 °C, 220.6 bar, X_{NaCl}=0). The critical curve or locus of critical points links the critical point of H_2O

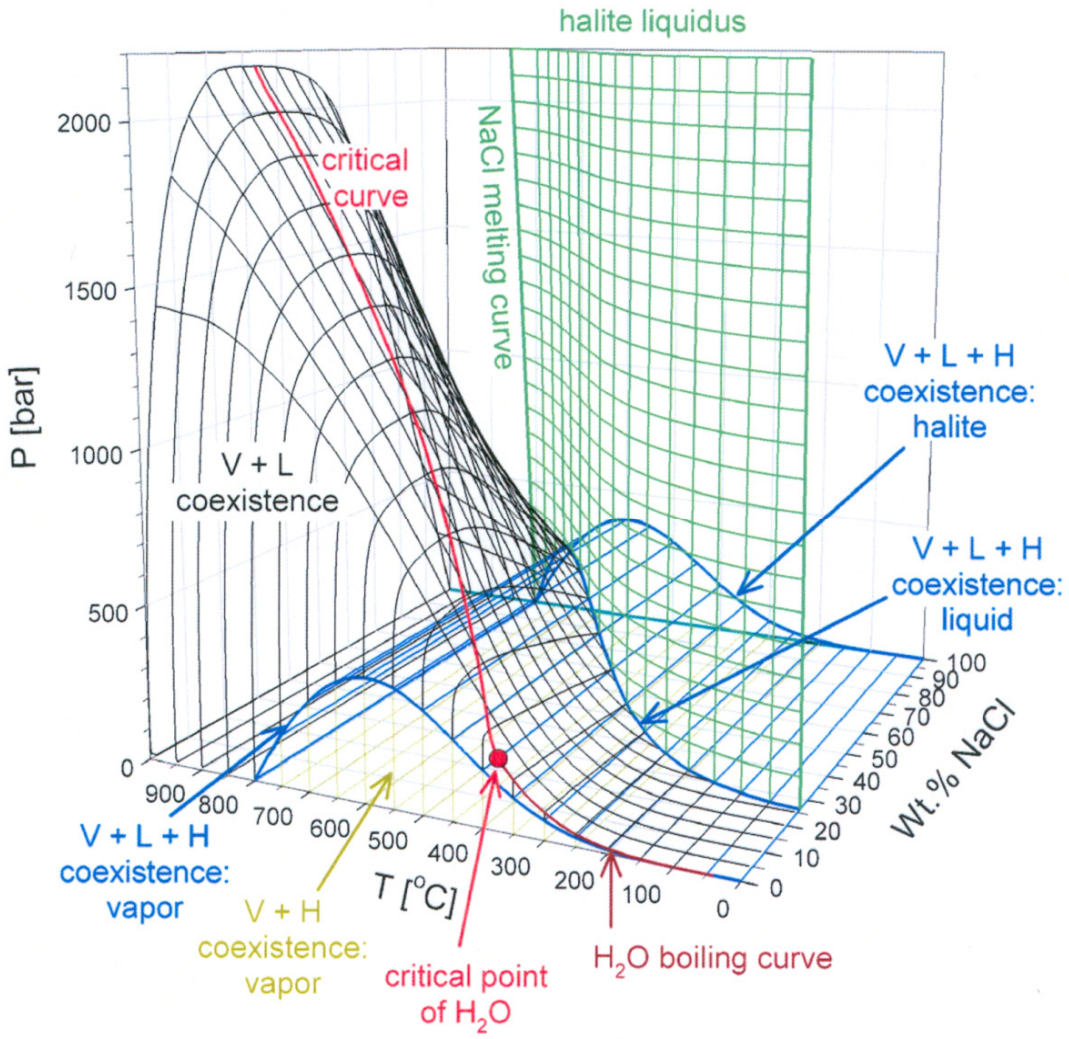

Figure 1.4 Pressure-temperature-salinity (P-T-X) diagram for the NaCl-H_2O system. [from *Driesner and Heinrich,* 2007]

with the critical point of NaCl (~3568 °C, ~182 bar, X_{NaCl}=1). The crest of the V+L coexistence region is formed by the boiling curve of H_2O at temperatures below the critical point of H_2O and by the NaCl-H_2O critical curve at higher temperatures. Either single phase liquid, single phase vapor, or supercritical fluid, is above the solvus. The vapor + liquid + halite (V+L+H) coexistence surface is the lower pressure boundary for V+L coexistence, and the upper pressure

boundary for V+H coexistence. The halite liquidus is the surface along which a fluid is saturated with halite. The halite will precipitate if more NaCl is added into the fluid.

The goal of this study is to obtain a better understanding of phase separation in seafloor hydrothermal systems by constructing numerical simulations of two-phase flow using the phase equilibrium and thermodynamic and transport properties of NaCl-H_2O as an analog for hydrothermal fluids in sub-seafloor hydrothermal systems. To limit the discussion, I consider a seafloor pressure of 25 MPa and consider various crustal permeabilities and bottom temperature distributions. Because of the time series vent fluid salinity measurements (Figure 1.3) that are available for EPR 9°50′ N, I also discuss the relationship of the numerical simulations to this hydrothermal system. Basic features of this system are described in the next section.

1.3 Hydrothermal system at East Pacific Rise 9°50'N

Hydrothermal and magmatic activity between 9°-10°N on the East Pacific Rise (EPR) has been studied extensively since the 1980's period. Some key features determined since that time, include the AMC depth [*Detrick et al.*, 1987], the hydrothermal vent distribution [*Haymon et al.*, 1991, 1993], the vent fluid geochemistry [*Von Damm*, 2004], and advective heat output [*Ramondenc et al.*, 2006]. Further discussions are in the Chapters 3.3 and 3.4. In particular, the hydrothermal systems at 9°50'N (Figure 1.5) lie at a depth of ~2500 m below sea level, which corresponds to a seafloor pressure of ~ 25 MPa. Seismicity patterns suggest that the circulation may be largely along axis [*Tolstoy et al.*, 2008]. The magma chamber is ~ 1.5 km long along axis [e.g., *Tolstoy et al.,* 2008], and 1.5 km below the seafloor [*Detrick et al.*, 1987]. Assuming the hydrothermal activity is confined to a region above the AMC, the hydrothermal system depth is 1.5 km. As mentioned in section 1.3, the vent fluid salinity of Bio9 and P vent at this site has

evolved in a similar pattern, but they also have remarkably different salinities in 1996, although they are only separated by ~60m.

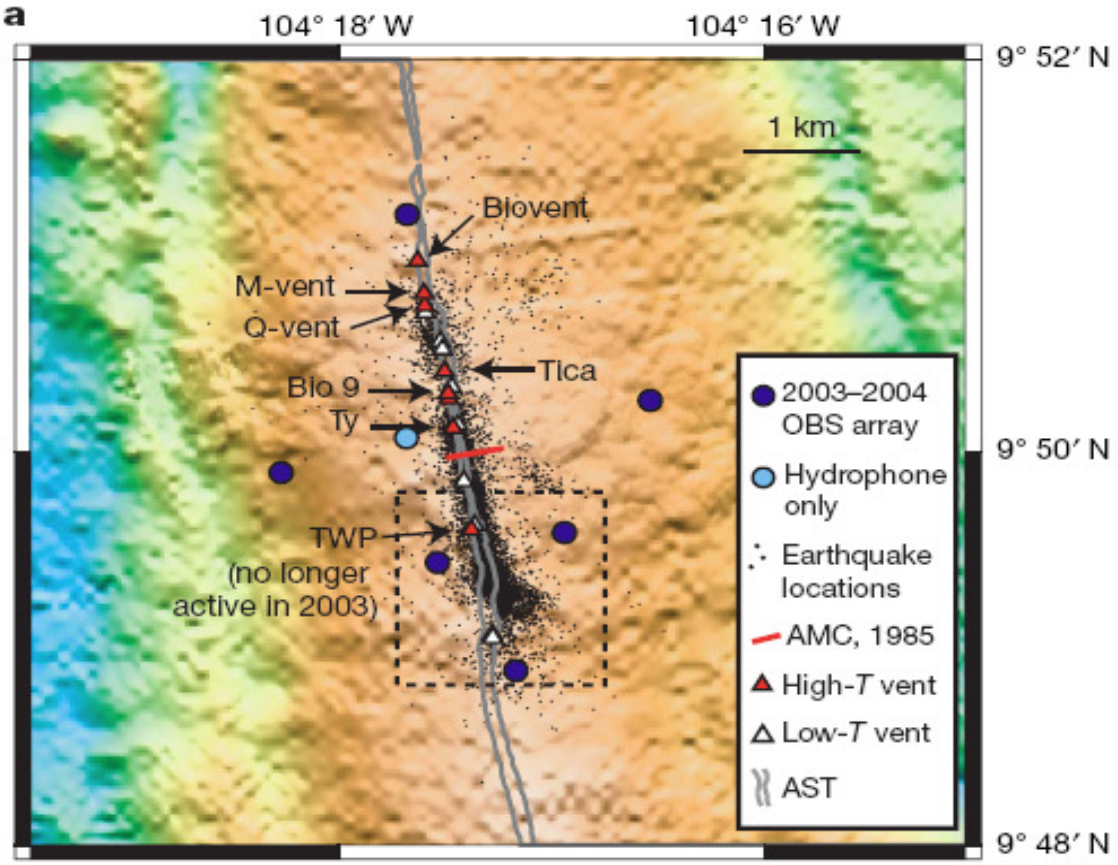

Figure 1.5 Locations of various hydrothermal vents and seismicity on the East Pacific Rise at 9°50'N [from *Tolstoy et al.,* 2008].

This thesis describes results of numerical simulations of two-phase flow in a seafloor hydrothermal system. In Chapter 2, I discuss previous modeling of two-phase flow in seafloor hydrothermal systems, and in particular I describe the main features of the FISHES code that is used in these simulations. In Chapter 3, which is the heart of this thesis, I discuss the numerical simulation and their application to the EPR 9°50′ N hydrothermal system. This chapter constitutes a paper to be submitted to the Journal of Geophysical Research. In Chapter 4, I

provide some recommendations for future work. The Appendix includes useful Fortran and Matlab codes used in the thesis and some additional model results.

CHAPTER 2: PREVIOUS WORK AND THE FISHES CODE

2.1 Previous work

Hydrothermal system modeling stems from the fundamental work of *Horton and Rogers* [1945] and *Lapwood* [1948], who derived the critical Rayleigh number for the onset of convection in a porous layer heated from below. *Mckenzie* [1967], *Sclater and Francheteau* [1970] and *Parker and Oldenburg* [1973] developed mathematical models of conductive heat flux through seafloor; however, the discrepancy between observed and predicted heat flow suggested heat loss by submarine hydrothermal convection systems [e.g., *Elder*, 1965; *Lister*, 1972]. Later mathematical models of seafloor hydrothermal systems were developed [e.g., *Bodvarsson and Lowell,* 1972; *Lister,* 1974; *Strens and Cann*, 1982; *Lowell,* 1975; *Fehn and Cathles* 1979, 1986; *Fehn et al.,* 1983]. The discovery of high-temperature black smoker emissions [*Spiess et al.*, 1981] ushered in a new generation of models of hydrothermal convection at ridge crests [e.g., *Brikowski and Norton*, 1989; *Lowell and Burnell*, 1991; *Lowell and Germanovich*, 1994, 2004; *Wilcock,* 1998]. Those numerous studies had generally considered high temperature thermal convection of a single component (H_2O), single phase fluid. Many of these studies used the Boussinesq approximation, in which density terms are only considered in the buoyancy term and neglected elsewhere.

Hydrothermal circulation models including boiling were first developed in late 1990s [e.g., *Zyvoloski et al.,* 1997, 1998; *Bower and Zyvoloski,* 1997; *Lowell and Xu,* 2000]. Some studies used pure H_2O as a proxy for seawater [*Ingebritsen and Hayba,* 1994; *Lowell and Xu*, 2000; *Jupp and Schultz*, 2000; *Coumou et al.*, 2006], and other studies assumed a computational cell filled entirely with either vapor or liquid phase [*Cathles,* 1977; *Fehn and Cathles,* 1979,

1986; *Fehn et al.,* 1983]. Still others used properties of seawater but averaged the properties of the two phases [*Wilcock,* 1998; *Foutaine and Wilcock*, 2007], or assigned identical fluid properties (except for density) for each phase [*Kawada et al.,* 2004].

Hydrothermal modeling using phase equilibrium and thermodynamic properties of a NaCl-H_2O fluid has begun only recently. *Bai et al.* [2003] considered a one-dimensional heat pipe model in a NaCl-H_2O fluid, finding that a brine layer forms at the base of the system while vapor ascends towards the surface. *Lewis and Lowell* [2004] took a 2-D approach for two-phase flow of seawater near an igneous dike but treated heat transport by conduction only. *Fontaine et al.* [2007] study the effects of different permeability structures, and find that shallow high permeability layers decrease effluent temperatures and a vertically extensive impermeable zone between upflow and downflow zone increases effluent temperatures and salinities. Complex Systems Platform (CSMP++) [*Geiger et al.,* 2006a, 2006b; *Matthäi et al.,* 2007; *Coumou,* 2008; *Coumou et al.,* 2009] and Fully Implicit Seafloor Hydrothermal Event Simulator (FISHES) [*Lewis and Lowell,* 2009a, 2009b] have been developed to simulate high temperature phase separation in NaCl-H_2O fluids. *Lewis and Lowell* [2009b] show examples of two phase flow simulation of seawater using constant temperature boundary for 1-D heat pipe model, 2-D single-pass model and cellular convection model. *Coumou et al.* [2006] show that plume splitting in a single phase hydrothermal convection system due to temperature-dependent viscosity variations may cause spatial and temporal variation of hydrothermal venting. *Coumou et al.* [2008a] show that at near-critical conditions, two-phase convection can be more efficient in heat transport than single-phase convection. *Coumou et al.* [2008b] performed high-resolution three-dimensional simulation of seafloor hydrothermal systems using the properties of pure H_2O to show the self-

organized pipe-like plume structures. *Coumou et al.* [2009] argued that vent fluid salinity variation may result from plume splitting or the dynamic effects of phase separation.

2.2 FISHES

FISHES solves the equations that describe conservation of mass, momentum, energy, and salt in a hydrothermal system using the properties of NaCl-H_2O. Equations for the conservation of mass, momentum and energy have been derived by *Faust and Mercer* [1979] who discussed two-phase flow in pure H_2O. The equation for the conservation of salt is from *Bai et al.* [2003]. The specific form of these equations is as follows:

The equation of mass conservation is

$$\frac{\partial(\phi\rho)}{\partial t} + \nabla \cdot (\rho_v \vec{v}_v + \rho_l \vec{v}_l) = 0 \tag{1}$$

where ϕ is the porosity, ρ is the bulk density of the fluid or the density of each phase, $\vec{v}$ is the Darcian velocity, and the subscripts *v* and *l* refer to the vapor and liquid phases, respectively.

The equation of momentum conservation is

$$\vec{v}_v = -\frac{Kk_{rv}}{\mu_v}(\nabla P - \rho_v g \nabla z)$$
$$\vec{v}_l = -\frac{Kk_{rl}}{\mu_v}(\nabla P - \rho_l g \nabla z) \tag{2}$$

where K is the permeability, k_r is the relative permeability, P is the pressure, z is the depth, μ is the dynamic viscosity, g is the gravitational acceleration.

The equation of energy conservation is

$$\frac{\partial}{\partial t}[\phi\rho h + (1-\phi)\rho_r c_r T] + \nabla \cdot (\rho_v h_v \vec{v}_v + \rho_l h_l \vec{v}_l) = \nabla \cdot (\lambda_m \nabla T) \tag{3}$$

where h is the specific enthalpy of the fluid, T is the temperature, λ_m is the effective thermal conductivity of the medium, and the subscript r refers to the rock; ρ and h without subscripts refer to bulk quantities.

The equation of salt conservation is

$$\frac{\partial}{\partial t}(\phi\rho X) + \nabla \cdot (\rho_v \vec{v}_v X_v + \rho_l \vec{v}_l X_l) = \nabla \cdot (\phi\rho_l D \nabla X_l + \phi\rho_v D \nabla X_v) \tag{4}$$

where X is the bulk salinity (wt%) and D is the salt chemical diffusivity (taken to be 1×10^{-9} m^2/s).

The numerical code FISHES [*Lewis and Lowell*, 2009a, 2009b] uses the finite volume method [*Patankar*, 1980] to solve the above equations subject to applied boundary and initial conditions. The densities, salinities, and enthalpies of the fluid phases as functions of P-T-X are evaluated via linear interpolation between values in thermodynamic lookup tables. The bulk density from 300 to 800 °C and the salinity and density on the upper boundary of the two-phase region are based on the work of *Anderko and Pitzer* [1993], and the bulk density from 0 to 300 °C is based upon the work of *Archer* [1992]. The specific enthalpy is compiled using the framework of *Tanger and Pitzer* [1989] and Archer's Program. The salinity on the salt saturated vapor surface is obtained using the correlation equation from *Palliser and Mckibbin* [1998]. More details can be found in *Lewis* [2007] and *Lewis and Lowell* [2009a]. These tables are valid for pressures between 85 and 1000 bars, temperatures between 0° and 800 °C, and salinities between 0 and 100 wt% NaCl. As described by *Lewis and Lowell* [2009a] FISHES has been benchmarked against the thermal convection-diffusion solution in the single-pass one-phase system, the Elder problem [*Elder*, 1967], the problem of fluid extraction from a one-dimensional

two-phase horizontal pipe and an analytic solution for a one-dimensional vertical salt pipe simulation. *Lewis and Lowell* [2009a] describe additional details of the numerical formulation, equation of state and benchmarking; and *Lewis and Lowell* [2009b] contains example simulations for both single-pass heterogeneous permeability structures and for cellular convection in a homogeneously permeable porous rectangular porous system.

The code FISHES and User's Manual are available for download at http://www.geophys.geos.vt.edu/rlowell/kaylal/. The code includes algorithms to test for conservation of mass during each time step. If the local mass percent error is greater than the user defined criteria, the code will automatically halve the time step and redo the calculation for that specific time slice, and then the local mass percent error will be checked again. This process is repeated until the local mass percent error becomes smaller than the allowance or the time step becomes smaller than the minimum value set by the user, which will terminate the calculation. In addition, the equations are solved in fully implicit form, which means we always use most recent values. All information compiled during running the code is saved in the FISHES.log file, which can be examined to assess the quality of the simulation.

In this thesis I consider the V+L coexistence region and liquid region in P-T-X diagram, which typically occurs in seafloor hydrothermal systems. In particular we consider the region between 25 and 45 MPa, and 0 to 500 °C, for reasons described below. With a fixed seafloor pressure of 25 MPa, the highest pressure corresponds to a depth of 2 km below the seafloor assuming a hydrostatic pressure gradient with a density of 1g/cm^3. Conductive heat loss of the vent fluid and the mixing process cause measured vent temperatures to be lower than the maximum temperature of subseafloor hydrothermal alteration processes; also the relatively high dissolved SiO_2 concentrations characteristic of many vent fluids at SJDF (Southern Juan de

Fuca), EPR and MAR require temperature higher than 400 °C if subsurface pressures are less than 50 MPa [*Seyfried et al.*, 1991]. Additionally, vent fluid chloride content requires phase separation in the sub-seafloor, which requires T > 440 °C at a bottom pressure of 40 MPa [*Bischoff and Pitzer,* 1989].

CHAPTER 3: The dynamics of two-phase hydrothermal systems at a seafloor pressure of 25 MPa: Application for EPR 9 ° 50' N[1]

3.1. Introduction

3.1.1. Vent fluid salinity and phase separation of seawater

Hydrothermal circulation at oceanic spreading centers is a complex process in which cold seawater enters the crust, is heated as it flows downward and horizontally near the top of the sub-axial magma chamber (AMC), reacts with crustal rocks, and then rises toward the seafloor as a result of its buoyancy where it discharges as hot (~ 350-400 °C) metal-laden fluid through vent chimneys and sulfide structures on the seafloor. One of the most striking features of the hydrothermal vent fluids is that their salinity differs significantly from seawater.

In Figure 3.1 vent fluid chlorinity is shown as wt% NaCl for hydrothermal fluids at a number of different hydrothermal sites. Seawater is assumed to be approximated by a 3.2wt% NaCl-H_2O solution [e.g., *Bischoff and Rosenbauer*, 1984]. Vent fluid salinities shown in Figure 3.1 range from about 0.2wt% to about 5.5wt%, or from less than 10% to approximately 200% of normal seawater salinity. As shown in Figure 3.1, more data are available for EPR 9-10° N and MEF than elsewhere, but the data are still too limited to provide a clear overview of the entire evolution of vent fluid salinity with time. In part, this is a result of the relatively short, two-decade history of vent measurements. It is also a result of the relatively infrequent sampling rate at most vent sites. An exception is *Larson et al* [2007] that measured both vent fluid temperature and salinity at the Main Endeavor Field on the Juan de Fuca (JDF) ridge in the NE Pacific with

---

[1]This chapter is essentially a paper of this title authored by Han et al. to be submitted to JGR-solid earth

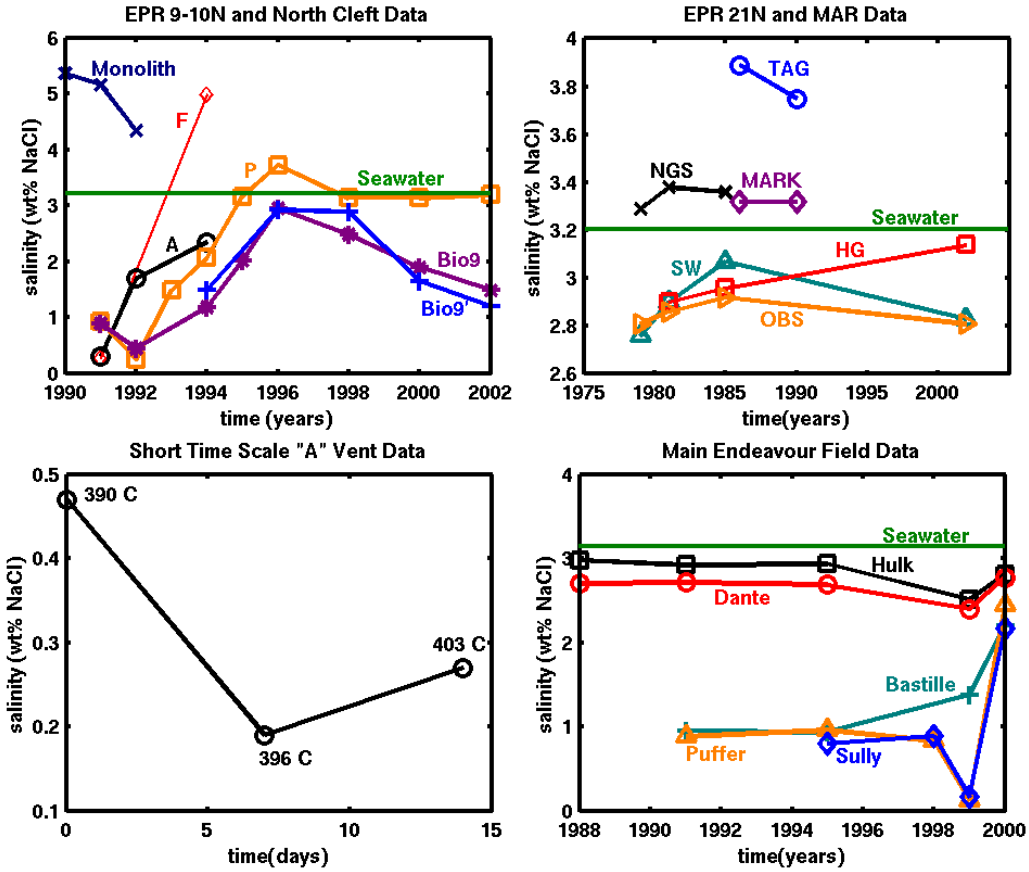

Figure 3.1 Summary of vent fluid salinity data from the literature. In the upper left panel, Monolith is a North Cleft site on the JDF; the others are from EPR 9-10˚N. In the upper right panel, TAG and MARK refer to MAR sites; the others refer to EPR at 21˚N. The lower left panel is a two-week time series of vent fluid salinity and temperature at "A" vent at 9˚N EPR. The lower right panel shows sites from the Main Endeavor Vent Field, JDF. Data prior to 1995 are taken from *Von Damm* [1995]. More recent data from 9° N EPR are from *Von Damm* [2004] and those from 21°N EPR are from *Von Damm et al.* [2002]. More recent data from Main Endeavor are from *Lilliey et al.* [2003]. [from *Lewis and Lowell*, 2004].

sampling rate as high as 1 min^{-1} for two months. Although these data showed rapid daily changes in vent fluid salinity and temperature, the changes are mainly due to tides, which are not included in our model. We have also not considered external perturbation arising from magmatic and tectonic events, such as dike emplacement and earthquakes. It is clear from the plots in Figure 3.1, however, that most vent fluids at the EPR and MEF are below seawater salinity (a notable exception being P vent at EPR 9°50′ N between 1995 and 1998) and that vent fluid salinity may

change markedly on a time scale of years or less. Salinity may vary between even closely spaced vents at the same hydrothermal site, such as Bio9 and P vent at EPR 9°50′ N, which are separated by approximately 60m [*Von Damm*, 2004]. Different vents within the same vent field may exhibit somewhat similar temporal variations.

Although differences between vent fluid salinity and seawater may result in part from the precipitation and dissolution of a Cl-bearing mineral in the subsurface [*Seyfried et al.*, 1986], it is widely acknowledged that the primary cause is subsurface phase separation of seawater into vapor and brine phases [e.g., *Berndt and Seyfried*, 1990; *Von Damm et al*., 1997, 2002; *Von Damm*, 2004]. Oceanic spreading centers with seafloor depths ranging between approximately 1500 and 3500 m correspond to seafloor pressures of approximately 15-35 MPa. For a fluid of seawater composition, phase separation would occur near the seafloor, provided the temperature was above 342°C at a pressure of 15 MPa, and at 425°C at a pressure of 35 MPa [*Bischoff and Pitzer*, 1989]. If we further assume that a system of fractures extends into the subsurface to near the top of the sub-axial magma chamber, pressures at depth beneath the high-temperature vents would increase by approximately 8.5 MPa per km, thus higher temperatures are required for phase separation at depth. For example, for a magma chamber approximately 1.5 km below the seafloor and a seafloor pressure of 25 MPa, corresponding to the EPR near 9°50′ N, phase separation near the seafloor would occur at approximately 387 °C, and phase separation near the top of the AMC would occur at approximately 435 °C [e.g., *Bischoff and Pitzer*, 1989].

The relationship between phase separation and pressure, temperature and salinity is illustrated by the NaCl-H_2O phase diagram (Figure 3.2). The phase diagram is separated into 5 regions, including a vapor + halite (V+H) coexistence region, a vapor + liquid (V+L) coexistence region, and a liquid + halite (L+H) coexistence region on the low temperature and/or low salinity

side of halite liquidus surface. Two of the regions contain only a single phase. The liquid (or single phase fluid with liquid-like density) region occurs on the high pressure and/or high salinity side of V+L coexistence region, and the vapor (or single phase fluid with vapor-like density) region occurs on the low pressure and/or lower salinity side of V+L coexistence region. The boundary between vapor and liquid for H_2O is defined by a line in PT space, whereas the liquid-vapor coexistence region for NaCl-H_2O is defined by a volume in P-T-X space. The vapor-liquid

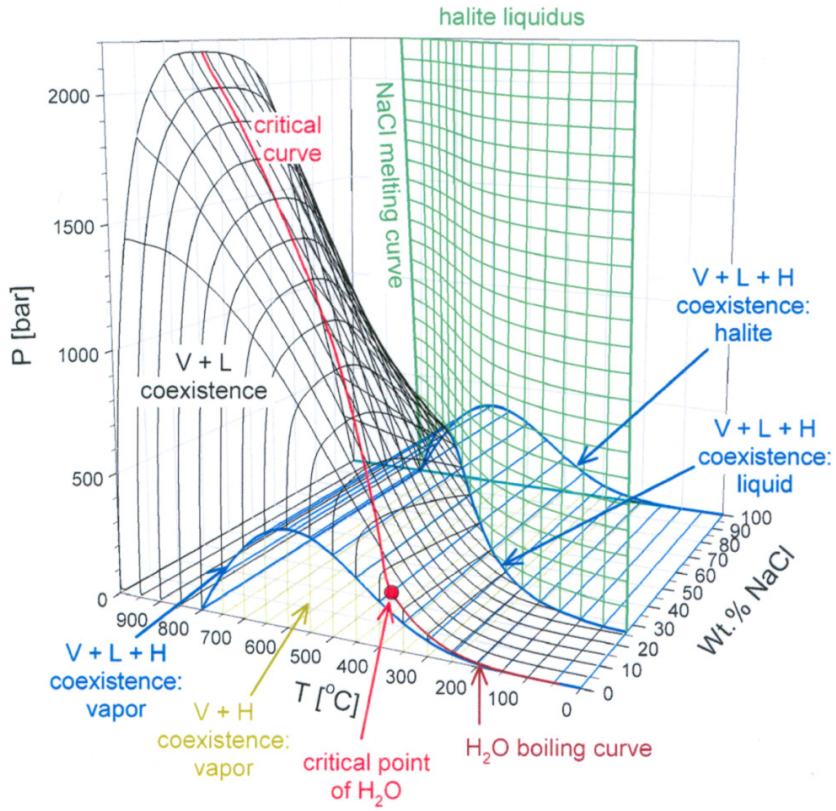

Figure 3.2 Pressure-temperature-salinity (P-T-X) diagram for the NaCl-H_2O system. [from *Driesner and Heinrich*, 2007]

critical point for H_2O denotes the conditions (pressure and temperature) above which distinct liquid and gas phases do not exist. The boiling curve for H_2O terminates at the H_2O critical point (373.976 °C, 220.6 bar, X_{NaCl}=0). The critical curve or locus of critical points links the critical

point of H_2O with the critical point of NaCl (~3568 °C, ~182 bar, X_{NaCl}=1). The crest of the V+L coexistence region is formed by the boiling curve of H_2O at temperatures below the critical point of H_2O and by the NaCl-H_2O critical curve at higher temperatures. Either single phase liquid, single phase vapor, or supercritical fluid, is above the solvus. The vapor + liquid + halite (V+L+H) coexistence surface is the lower pressure boundary for V+L coexistence, and the upper pressure boundary for V+H coexistence. The halite liquidus is the surface along which a fluid is saturated with halite. The halite will precipitate if more NaCl is added into the fluid. In this paper we consider the V+L coexistence region and liquid region in the P-T-X diagram, which typically occurs in seafloor hydrothermal systems. In particular we consider the region between 25 and 40 MPa, and 0 to 500°C. With a fixed seafloor pressure of 25 MPa, the highest pressure corresponds to a depth of 2 km below the seafloor assuming a hydrostatic pressure gradient with a density of 1g/cm^3. Conductive heat loss of the vent fluid and the mixing process cause measured vent temperatures to be lower than the maximum temperature of sub-seafloor hydrothermal alteration processes; also, the relatively high dissolved SiO_2 concentrations characteristic of many vent fluids at SJDF (Southern Juan de Fuca), EPR and MAR requires temperature higher than 400 °C if subsurface pressures are less than 50 MPa [*Seyfried et al.*, 1991]. Additionally, vent fluid chloride content requires phase separation in the sub-surface, which requires T > 440°C at a bottom pressure of 40 MPa [*Bischoff and Pitzer,* 1989].

Conceptually, cold seawater enters the crust at the seafloor and flows downward. Near the top of the AMC the fluid begins to flow horizontally and the fluid continues to be heated. Under these conditions seawater separates into a low-salinity, low-density vapor phase and high-salinity, high-density brine phase. The high-density brine phase will tend to remain at the bottom of the convecting layer, while the low-density vapor phase fluid will flow upwards as a result of

its buoyancy, mix with the surrounding fluids and vent at the seafloor. These vapor derived fluids at the vents are called VDF for short in the later text. During active phase separation, the brine layer will grow in volume at the bottom of the system; and when the brine layer has grown to some extent, thermal perturbations related to cooling and heating of the plume at the bottom will drive some brine-phase fluid upwards. The ascending brine phase fluid will also mix with the nearby fluids, and may produce a vent fluid with salinity greater than seawater. In contrast, these brine derived fluids are called BDF for short in the following text. The phase separation and mixing process results in hydrothermal vent fluids with salinities different from seawater; and the vent fluid salinity may vary in both space and time.

The hydrological system at oceanic spreading centers is not well understood. The strong north to south pattern of decreasing vent fluid salinity at the MEF on the Juan de Fuca Ridge [*Butterfield et al.*, 1994; *Lilley et al.*, 2003] may indicate a 3-D circulation pattern corresponding to the changes in the subsurface conditions. However, seismicity patterns near the EPR 9°50' N region suggests that the circulation may be largely along axis [*Tolstoy et al.*, 2008]. Three-dimensional simulations of hydrothermal circulation including phase separation of seawater are not yet available. Consequently, we will present 2-D hydrothermal system simulations in this paper. In principle, the 2-D simulations could be considered to be either along axis or across-axis. For the EPR 9°50'N region, we will consider the simulation to represent an along axis system.

3.1.2. Previous models of two phase seafloor hydrothermal system

Hydrothermal circulation models including phase separation were first developed in 1990s [e.g., *Zyvoloski et al.,* 1997, 1998; *Bower and Zyvoloski,* 1997; *Lowell and Xu,* 2000]. Some studies took pure H_2O as a proxy for seawater [*Ingebritsen and Hayba,* 1994; *Lowell and*

Xu, 2000; *Jupp and Schultz*, 2000; *Coumou et al.*, 2006], and other studies assumed a computational cell occupied entirely by either a vapor or a liquid phase [*Cathles,* 1977; *Fehn and Cathles,* 1979, 1986; *Fehn et al.,* 1983]. Some workers used properties of seawater but averaged the properties of the two phases [*Wilcock,* 1998; *Foutaine and Wilcock*, 2007], or assigned identical fluid properties (except for density) for each phase [*Kawada et al.,* 2004].

Hydrothermal modeling using the phase equilibrium and thermodynamic properties of NaCl-H_2O began only recently. *Bai et al.* [2003] considered a one-dimensional heat pipe model in a NaCl-H_2O fluid, and found that a brine layer forms at the base of the system while vapor ascends towards the surface. *Lewis and Lowell* [2004] developed a 2-D model for two-phase flow of seawater near an igneous dike but treated heat transport by conduction only. *Fontaine et al.* [2007] implemented the Multidimensional Positive Define Advection Transport Algorithm technique to study the effects of different permeability structures, and found that shallow high permeability layers decrease effluent temperatures and that a vertically extensive impermeable zone located between the upflow and downflow zones increases effluent temperatures and salinities.

Complex Systems Platform (CSMP++) [*Geiger et al.,* 2006a, 2006b; *Matthäi et al.,* 2007; *Coumou,* 2008; *Coumou et al.,* 2009] and Fully Implicit Seafloor Hydrothermal Event Simulator (FISHES) [*Lewis and Lowell,* 2009a, 2009b] have been developed to simulate high temperature two-phase flow using the properties of NaCl-H_2O. *Lewis and Lowell* [2009b] show examples of two-phase flow simulation of seawater using a constant temperature boundary for the 1-D heat pipe, 2-D single-pass and cellular convection models. *Coumou et al.* [2006] showed that plume splitting during single phase hydrothermal convection occurs due to temperature-dependent viscosity variations, and this may lead to spatial and temporal variations in salinities during

hydrothermal venting. *Coumou et al.* [2008a] show that two-phase convection can be more efficient in heat transport than single-phase convection at near-critical conditions. *Coumou et al.* [2008b] performed high-resolution three-dimensional simulations of seafloor hydrothermal systems using the properties of pure H_2O to show the formation of self-organized pipe-like plume structures. *Coumou et al.* [2009] argued that vent fluid salinity variations may result from plume splitting or the dynamic effects of phase separation.

In this paper, we present a series of 2-D simulations of two-phase flow in a homogeneous permeable rectangular system using the phase equilibrium and thermodynamic properties of NaCl-H_2O. The goal of these simulations is to explore the effects of permeability, circulation depth, and maximum bottom temperature on the behavior of the hydrothermal system. For simplicity we assume a constant seafloor pressure of 25 MPa that is similar to the pressure along portions of the fast spreading East Pacific Rise and on the ridge axis at the intermediate spreading Juan de Fuca Ridge (≈ 22 MPa).

3.2. Problem Formulation

3.2.1. Numerical Method

We use the numerical code FISHES [*Lewis and Lowell*, 2009a, 2009b] to simulate two-phase hydrothermal circulation at mid-ocean ridges. FISHES uses the finite volume method [*Patankar*, 1980] to solve the equations that describe conservation of mass, momentum, energy, and salt in NaCl-H_2O systems derived by *Faust and Mercer* [1979]. The densities, salinities, and enthalpies as functions of P-T-X are evaluated via linear interpolation between values in thermodynamic lookup tables. These tables are valid for pressures between 85 and 1000 bars, temperatures between 0° and 800°C, and salinities between 0 and 100 wt% NaCl. FISHES has

been benchmarked against the thermal convection-diffusion solution in the single pass system, the Elder problem [*Elder*, 1967], the problem of fluid extraction from a one-dimensional two-phase horizontal pipe [*Kissling,* 2005a, 2005b], and an analytic solution for a one-dimensional vertical salt pipe simulation [*Kissling,* 2005b]. *Lewis and Lowell* [2009a] describe details of the numerical formulation, equation of state and benchmarking. Additional details concerning the numerical methods are also given in Chapter 2.

3.2.2 Model geometry

Figure 3.3 shows the configuration of the 2-D sub-seafloor environment considered in this study, with seafloor pressure P = 25 MPa, seafloor temperature = 10 °C, and permeability $k = 10^{-13}$ m^2 within a two-dimensional rectangle 1 km × 3km that serves as the "basic model". The bottom temperature distribution Tbot is represented by a 1 km wide region above the AMC at the bottom center of the system in which the temperature is equal to MaxTbot (maximum temperature at the bottom) (see Table 3.1), and a region of linearly decreasing temperatures that extends from the ends of this central region to the left and right boundaries. For the basic model, the high temperature region is 425°C and decreases linearly to 300°C at the left and right boundaries. With this temperature distribution at the base, two-phase flow will occur near the base of the system above the high-temperature region, but fluid will remain in the liquid phase away from this region. Other simulations, involving various permeabilities, system depths, and MaxTbot, represent permutations of the basic model. Because the model geometry is symmetric about its center, we use only one-half of the system for computation to save computational time. Along the center line, we assume there is no lateral heat transfer or fluid flow. We ran a full space model, and the lateral heat transfer and fluid flow exist, but they don't affect the general results.

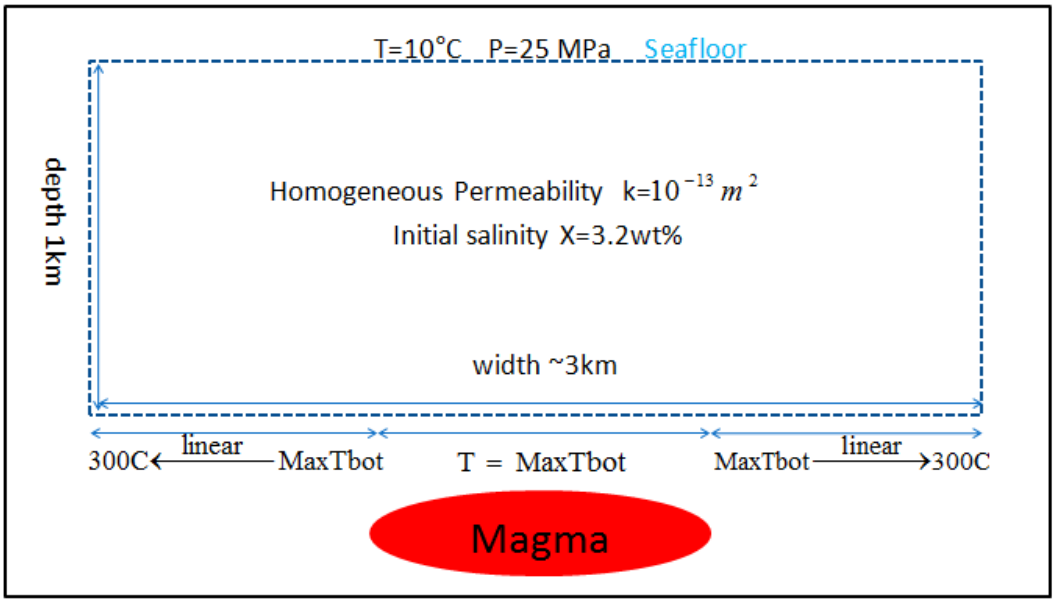

Figure 3.3 Schematic representation of the starting and boundary conditions used in simulations by FISHES. Seafloor pressure is 25 MPa, system is 1km deep, initial seafloor temperature is 10 °C, initial salinity is 3.2 wt%, and bottom temperature boundary is MaxTbot constant at the central 1 km wide region at the base of the system and decreases linearly to 300 °C on both sides.

To start the simulations, we assume that the salinity is initially homogeneous with a value of 3.2 wt%, corresponding to normal seawater. For most simulations, we also assume that the temperature initially increases linearly from the seafloor to the base of the system, and that the initial hydrostatic pressure distribution is then calculated from the temperature and salinity distribution. In order to examine the effect of the initial conditions, some simulations start with lower maximum bottom temperature, and then after the fluid flow and temperature fields are established, MaxTbot is increased to drive the flow into the two-phase regime.

Table 3.1 shows the starting conditions and system parameters used to explore the effects of permeability, system depth and bottom temperature on fluid flow. We begin by showing the

results of the basic model, which is simulation S1 in Table 3.1. Other simulations in Table 3.1, denoted by numbers will be designated in a similar fashion.

Table 3.1. Boundary conditions for the simulations

simulation	MaxTbot (°C)	Permeability (m^2) (-lg)	Single or two phase
S1	425	13	Two phase
S1*	425	13	Two phase
S2	400	13	Single phase
S3	450	13	Two phase
S4	475	13	Two phase
S5	400	12	Single phase
S6	425	12	Two phase
S7	450	12	Two phase
S8	475	12	Two phase
S9	425	14	Two phase

Values for constants used in FISHES are porosity $\emptyset = 0.1$, oceanic crust density $\rho_r = 2500$ kgm^{-3}, specific heat of oceanic rock $c_{pr} = 1000$ $JKg^{-1}K^{-1}$, thermal conductivity $K = 2.0$ $Jm^{-2}K^{-1}s^{-1}$. The seafloor pressure is 25 MPa, the system depth is 1km, and the magma chamber half width is 500m. Simulation S1 is the basic model, and is referred to as S1 below. Simulation S1* runs starting from the single phase steady state result of simulation S2.

3.3 Results

Figures 3.4 and 3.5 show the results from simulation S1. Figure 3.4 shows the vent fluid temperature and salinity as a function of time, while Figure 3.5 shows the isotherms and salinity distributions at different time slices.

The first plume, shown in yellow in Figure 3.4, reaches the seafloor around year 10 with a temperature of ~375 °C. This plume is located near the edge of the AMC where the bottom temperature increases to MaxTbot. At that time, a brine layer as wide as the AMC has formed at the bottom of the system with low salinity VDF rising in the plume above it. Approximately 5 years later, a second plume shown in blue in Figure 3.4 reaches the seafloor. At year 20, two plumes vent at the seafloor, and a vertical BDF region has developed at depth. Six years later, a

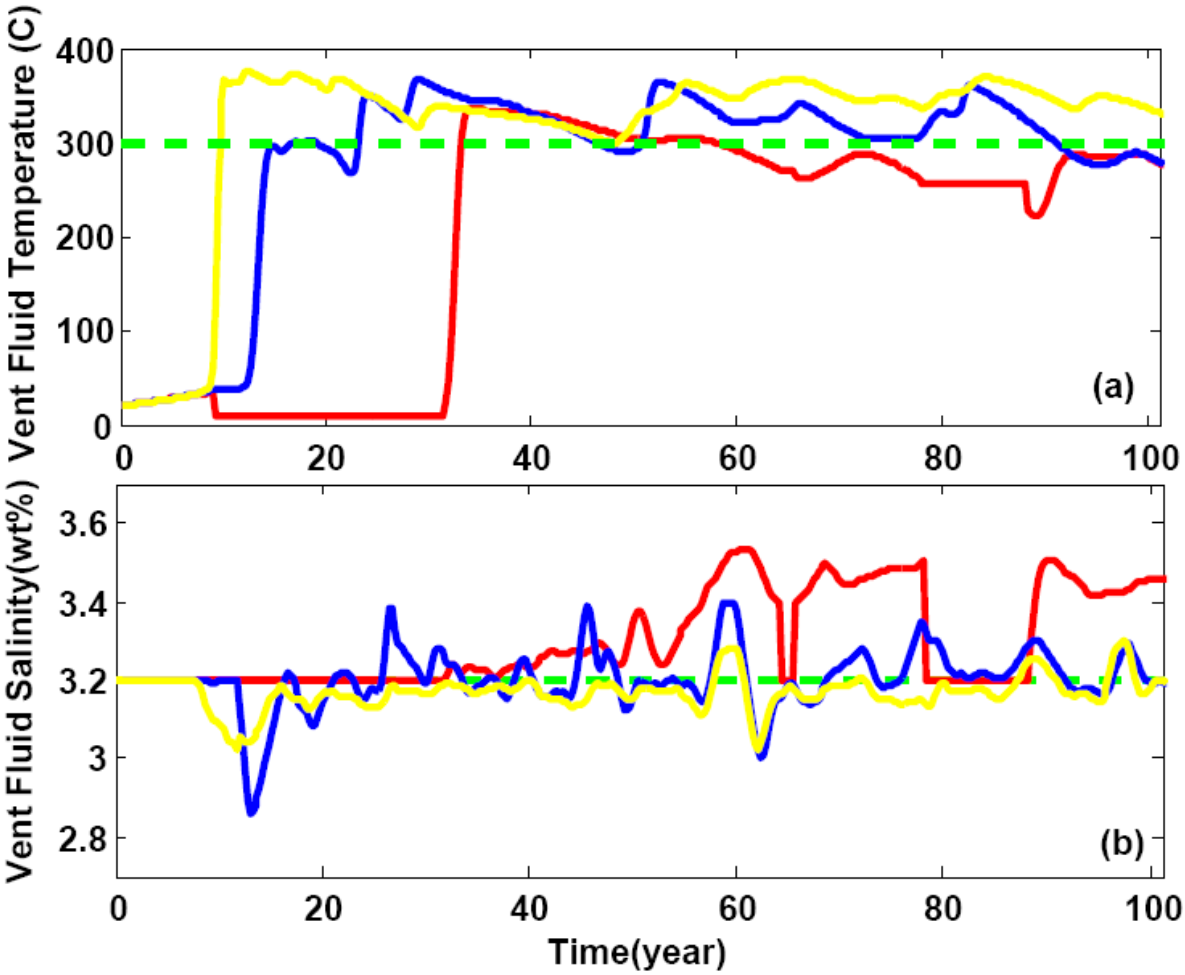

Figure 3.4 Vent fluid temperature and salinity evolution of simulation S1 with time in different plumes. Different colors show the result of different plumes in figure 3.5. Red is the left-most plume, blue is the second one from the left, and yellow is the third. Sampling rate is 4 times/year. Green dash lines show temperature of 300 °C and salinity of 3.2 wt%. The salinity plume usually reaches the seafloor a little earlier than the temperature plume.

pulse of BDF with salinity of 3.39 wt% vents at the seafloor 250 m from the left boundary. At year 35, the plume at the most-left in Figure 3.5 reaches the seafloor. The vent fluid temperature and salinity evolution of this plume are shown in red in Figures 3.4a and 3.4b, respectively. At year 60, all the three plumes are venting BDF while a broad region of upwelling vapor is present between the middle and right side plumes at depth. Note that the location of the 350 °C isotherm changes continuously over the 20 to 60 year time frame; and this fluctuation is reflected in the changing vent fluid temperatures in Figure 3.4a. These fluctuations likely result from cyclical heat transfer processes as a result of interactions between ascending plumes and fluid recharge. Simulation S1 shows that BDF or VDF could be rising from depth even though the other phase is venting at the surface at a given time and that a plume can switch from venting VDF to BDF and vice versa over time, as is shown in Figure 3.4b. Figure 3.4b also shows that not only are salinity fluctuations common in individual plumes, but also that VDF and BDF may vent simultaneously in different plumes. Note that vent fluid salinity in the plot follows the center of the plumes, which is the hottest location in the plume. In fact, because the plumes are relatively wide, VDF and BDF could vent simultaneously from different regions of the same plume. With the given pressure and temperature conditions on the boundaries in this simulation, the salinity varies between 2.86-3.54 wt%.

In spite of the dynamic environment at the bottom of the circulation cell where phase separation takes place, the minimum vapor salinity and the maximum brine salinity there are relatively stable throughout most of the simulation. Moreover, although the maximum brine salinity is ~15wt% and the minimum vapor salinity is ~1.6 wt% where phase separation occurs, maximum vent BDF salinity is ~3.54 wt% and the minimum vent VDF salinity is ~2.86 wt%. That is the vent fluid salinities are much closer to seawater salinity than those at depth, showing

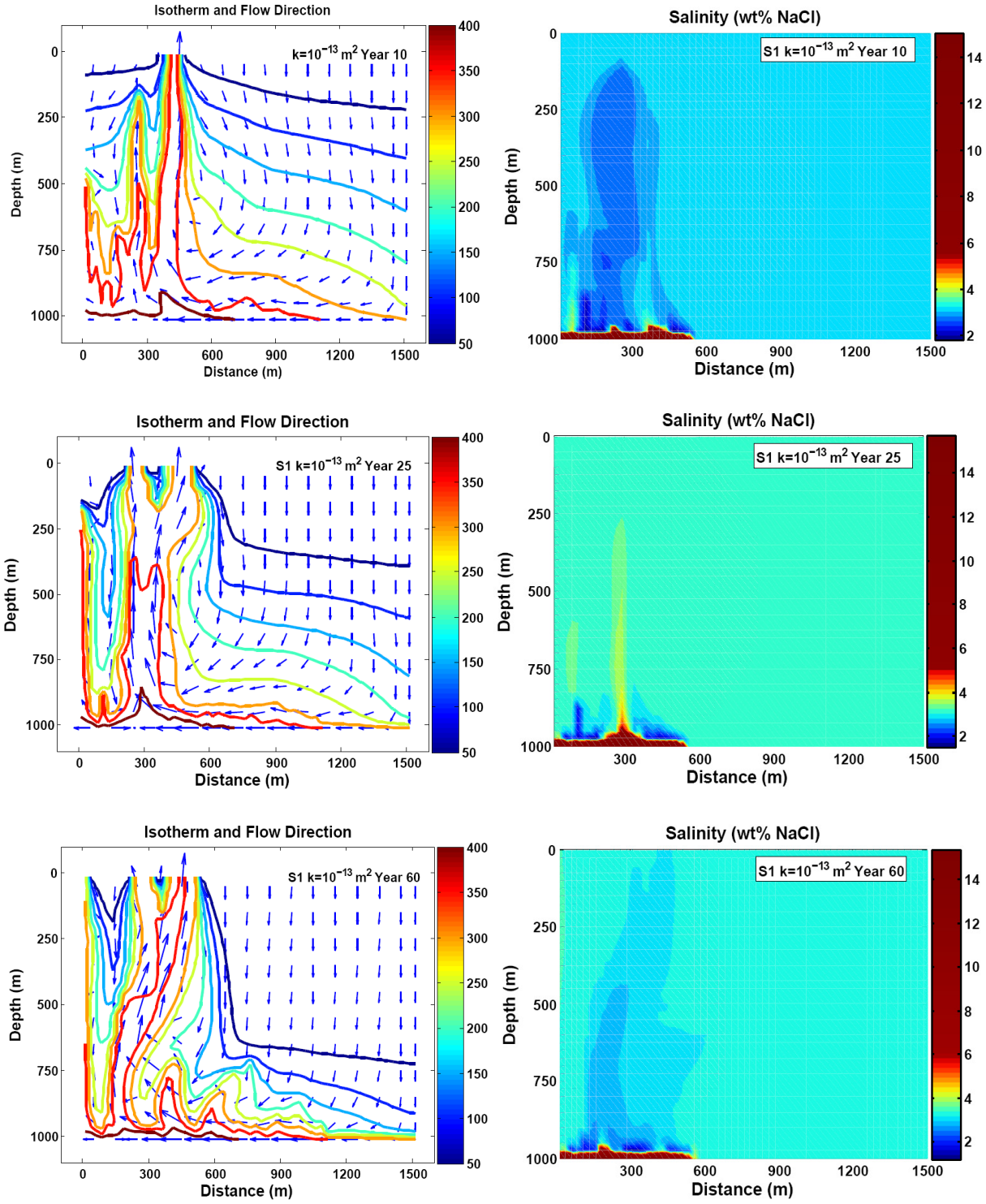

Figure 3.5 Isotherm and salinity distribution evolution with time of basic model S1. Flow vectors have been re-gridded and rescaled in order to show the flow direction clearly, so they only represent relative magnitude instead of actual velocity. Salinity color bar is also scaled to make VDF and BDF easier to recognize.

that the vent fluid is a mixture of phase separated fluid and seawater.

In addition to the continuous heating and phase separation of seawater in the region above the AMC, there is a broad recharge zone on the side with lower basal boundary temperatures. Isotherms are strongly depressed near the base of the recharge zone as cold seawater penetrates toward the bottom of the box. Recharge zones, in which cold seawater (~200 °C) penetrates rapidly to near the top of AMC, also occur between individual plumes. These localized recharge zones result in mixing between phase separated and normal seawater and partially explain the fluctuations of vent fluid temperature and salinity. These narrow but efficient recharge zones are similar to those observed in 3-D simulations of singe-phase hydrothermal circulation [*Coumou et al*., 2008].

3.3.1 The effect of starting conditions

In order to investigate the sensitivity of the results to starting conditions, we compare the two-phase results of simulation S1, which started with MaxTbot = 425°C with a similar simulation S1*, which started in the single phase with MaxTbot = 400°. This simulation ran until the flow field and temperature were established and then MaxTbot was gradually raised to 425°C over a five year period.

Figures 3.6 and 3.7 compare the results of S1 and S1*. Although there are some differences in the detailed thermal structure, Figure 3.7 indicates that many aspects of the mature plume structure are essentially independent of the starting conditions. For example, at year 50, both S1 and S1* have 3 plumes venting at the seafloor at almost the same locations. The isothermal structure in the broad cold recharge zone (on the right side) of S1 has not been depressed as strongly as that of S1* at that time, but it becomes nearly the same by year 100.

Figure 3.6 shows the vent fluid temperature and salinity of S1* as a function of time, while Figure 3.4 shows that of S1. Clearly, vent fluid temperature and salinity fluctuate in a similar pattern in both S1 and S1*. In addition, Table 3.2 shows that the maximum vent fluid temperature, T_{max}, the range of vent fluid salinity S_{min} and S_{max}, and the minimum vapor salinity and maximum brine salinity at the bottom of the system where phase separation occurs, and both simulations predict similar results. The comparison of S1 and S1* suggest that the results of FISHES code is relatively insensitive to the starting conditions.

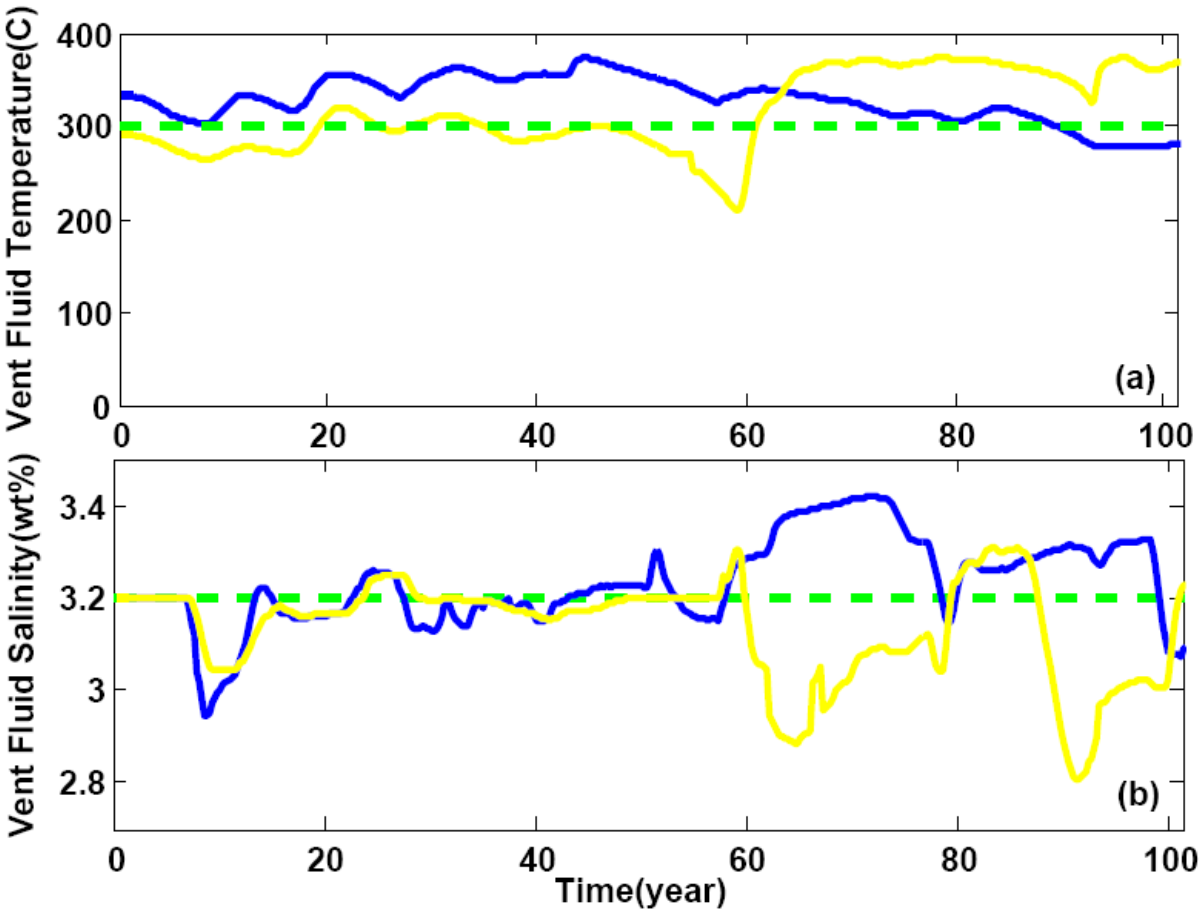

Figure 3.6 Vent fluid temperature and salinity evolution of simulation S1* with time in different plumes. Different colors show the result of different plumes. Blue is the second one from the left, and yellow is the third. Green dash lines show temperature of 300 °C and salinity of 3.2 wt%. The most-left plume is not shown in the plot because the new boundary condition mainly supports the plumes at the edge of magma chamber, and the most-left plume is not sufficiently heated any more. The sampling rate is 4 times/year.

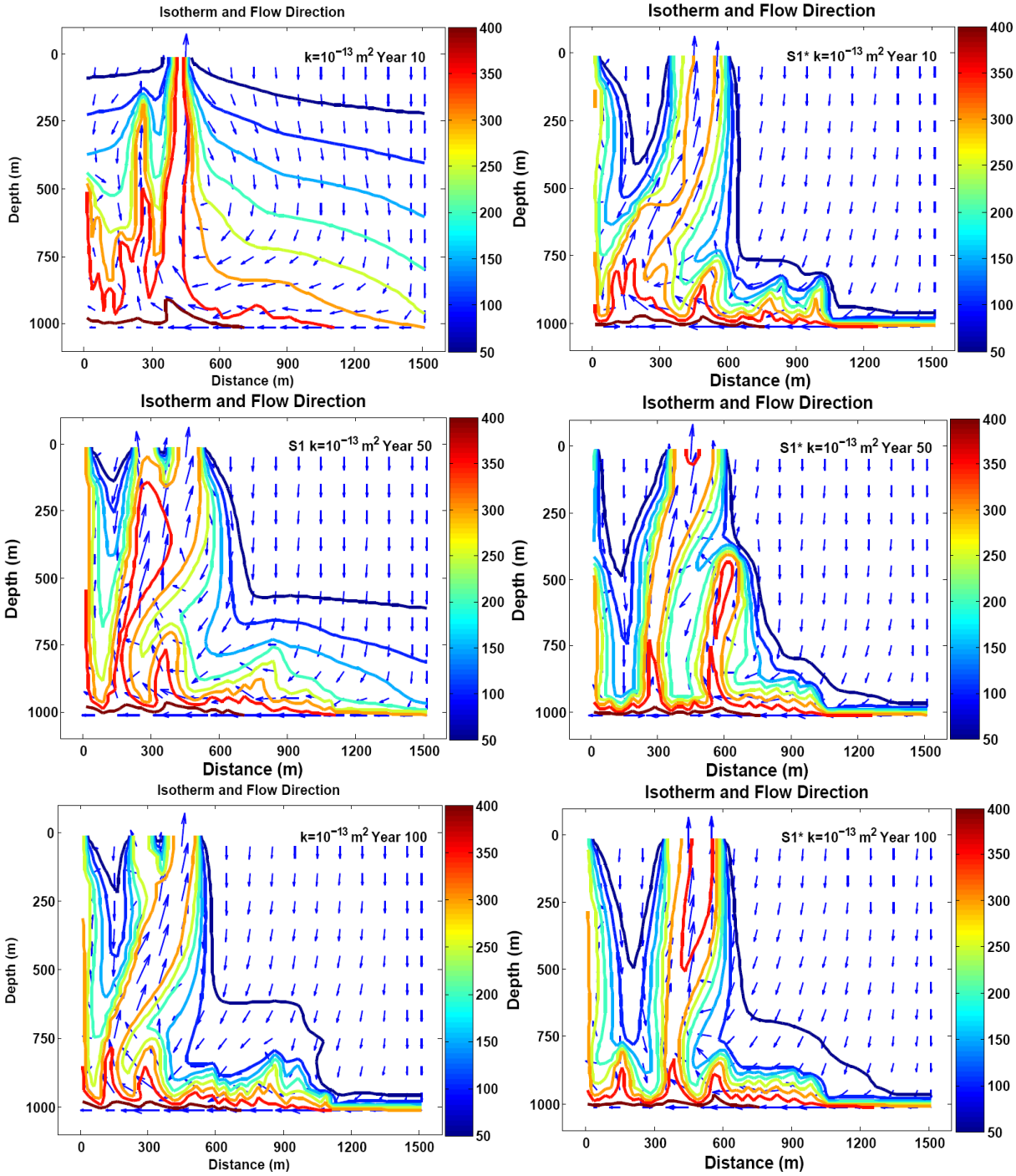

Figure 3.7. Comparison of simulation S1 and S1* at 10, 50 and 100 years. Simulation S1 which runs from normal initial condition is on the left and simulation S1* which runs from single phase steady state result is on the right. Flow vectors have been re-gridded and rescaled in order to show the flow direction clearly, so they only represent relative magnitude instead of actual velocity.

Table 3.2 Comparison of main features of simulations S1 and S1*.

Simulation	T_{max} (°C)	S_{min} (wt%)	S_{max} (wt%)	Max bottom brine salinity (wt%)	Min bottom vapor salinity (wt%)
S1	376	2.86	3.54	15.16	1.63
S1*	374	2.81	3.42	14.14	1.59

3.3.2 The effect of bottom temperature and permeability

To investigate the effects of MaxTbot on the evolution of vent fluid temperature and salinity and phase separation at the bottom of the system, we consider MaxTbot in the range from 400 to 475 °C and permeability of 10^{-13} and 10^{-12} m^2 for the same geometry and other boundary conditions as S1. In this range, most of the simulations shown in Table 3.1 are in the two-phase regime, and vent fluid temperatures are similar to those observed in seafloor hydrothermal systems.

In these simulations, single or multiple plumes vent at the seafloor after a certain time, and vent fluid temperature and salinity evolve with time in a manner similar to that shown in Figure 3.4. Because the temporal variations of both vent fluid temperature and salinity are not easily predictable, the mean vent fluid temperature of the hottest plume over time and the range of vent fluid salinity (i.e. minimum vent VDF salinity and maximum vent BDF salinity of the system) are used to compare the outputs of different models.

In order to depict the effect of MaxTbot and permeability on vent fluid temperature, Figure 3.8 shows the mean vent fluid temperature and standard deviation from the hottest plume during a simulation versus MaxTbot, for $k = 10^{-12}$ and 10^{-13} m^2, respectively. These simulations are labeled S2 through S8 in Table 3.1. Because it takes time for the hot fluid to reach the seafloor, only the time after the hot fluid (> 250 °C) reaches the seafloor is considered. Although

the hottest fluid temperature could be above 385 °C occasionally, the mean vent fluid temperature is below 365 °C. For both permeability values, as MaxTbot increases, surface vent

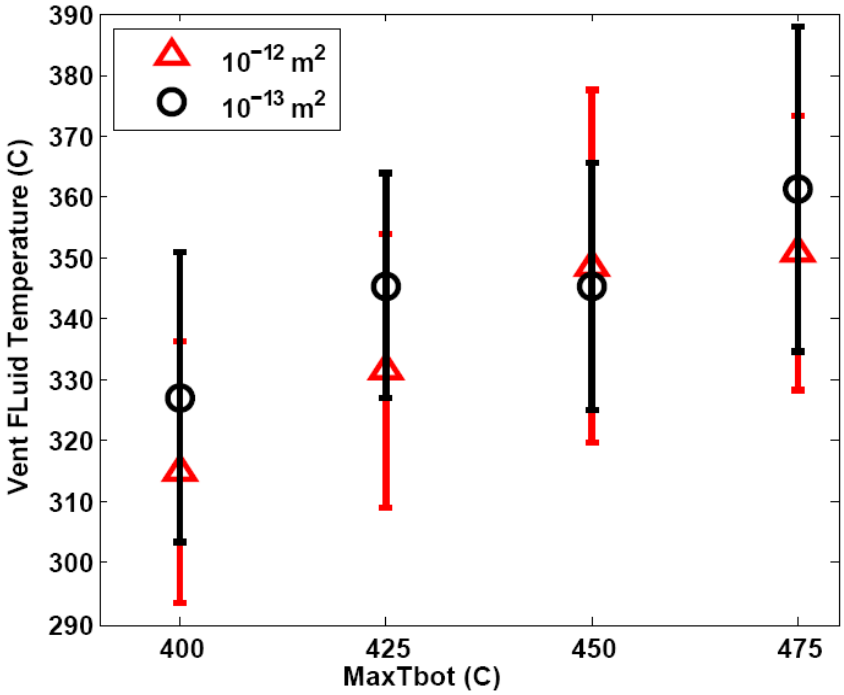

Figure 3.8 Vent fluid temperature as a function of MaxTbot at a seafloor pressure of 25 MPa and a system depth of 1km. Different symbols show the mean vent fluid temperature for different permeabilities: the red triangle refers to 10^{-12} m^2, and the black circle is 10^{-13} m^2. The error bar corresponds to the standard deviation of each sample.

fluid temperature also increases, but not as much as the bottom temperature. Although bottom temperature has a greater effect on vent fluid temperature than permeability, the temporal variability of vent fluid temperature shown by the standard deviation from the mean in Figure 3.8 suggests that subsurface permeability or bottom temperature cannot be deduced from the vent fluid temperature alone. These results are for a reasonably small cell size of 25 m on a side, and a simulation with 10 m cell size and a permeability of 10^{-12} m^2 yields slightly higher vent fluid temperatures [See Appendix B].

Phase equilibria (Figure 3.2) indicate that a higher MaxTbot will result in brine with higher salinity and vapor with lower salinity at the top of the AMC where phase separation

occurs, provided that the bottom pressure is the same. Similarly, in the early stages, the phase-separated fluids mix with surrounding normal seawater, which results in fluids with changing salinity. After several years, when a brine layer has formed at the bottom, the brine salinity at the bottom becomes stable in both space and time. However, the vapor resulting from phase separation does not remain at the bottom but rather arises to the surface with mixing, and the vapor salinity is affected by phase separation, brine layer deconstruction and horizontal circulation. As a result, the minimum vapor salinity, which is near the bottom, is only relatively stable in time. For example, in simulation S3 in Table 3.1, after 5 years the brine salinity (~38 wt%) above the AMC varies by less than 1 wt% with time and ~0.2 wt% with location, and the minimum vapor salinity of the system (~1.4 wt%) varies by ~0.5 wt% at most with time.

During the ascent of phase-separated fluid, mixing processes tend to return its salinity closer to that of normal seawater. In other words, mixing will increase VDF salinity and decrease BDF salinity. In order to show the effect of mixing on vent fluid salinity, minimum vent VDF salinity and maximum vent BDF salinity are selected to compare with fluid salinity at the bottom of the system as shown in Figure 3.9.

Similarly, simulations S1 to S8 are compared to explore the effect of MaxTbot at the same seafloor pressure of 25 MPa and system depth of 1 km. Simulation S2 and S5 are not considered because they are still in the single phase regime at a maximum bottom temperature of 400 °C. Also, for the same reason indicated in the discussion above, only the time period after a brine layer is formed at the bottom is considered for both bottom fluid salinity and vent fluid salinity. The mean and the standard deviation over time are calculated from highest brine salinity or lowest vapor salinity in each time slice, because they are appropriate representations of freshly phase separated fluid. The standard deviation of the bottom brine salinity is slightly smaller than

that of the bottom vapor salinity (note the different scale of the y axis) because of the relative stability of the brine layer. Figure 3.9 shows clearly that for different permeabilities and different MaxTbot values, even the maximum vent BDF salinity is still much smaller than the bottom

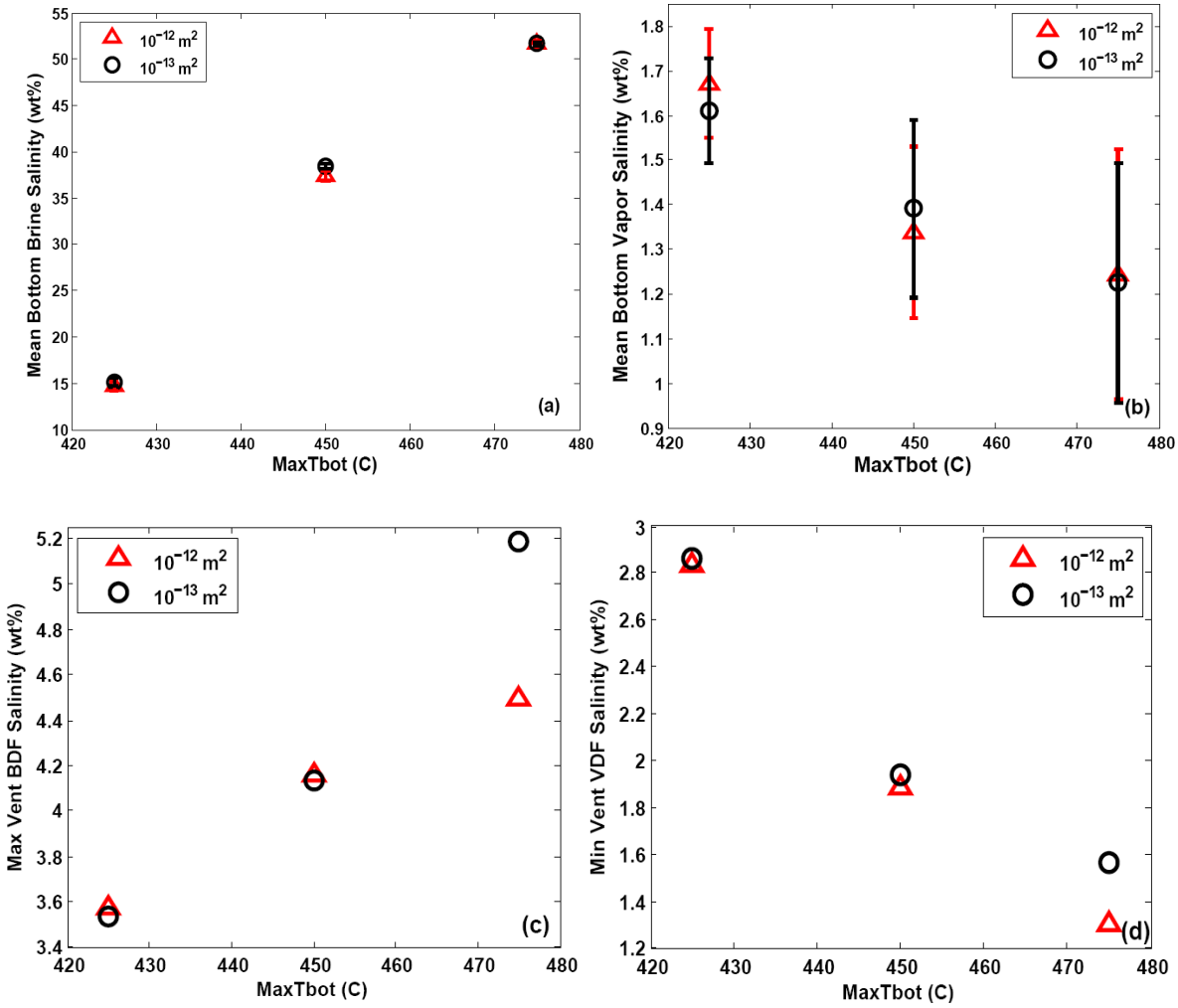

Figure 3.9 Fluid salinity at the top of the AMC and vent fluid salinity as a function of MaxTbot at a seafloor pressure of 25 MPa and a system depth of 1km. Different symbols show different permeabilities: the red triangle refers to 10^{-12} m^2, and the black circle is 10^{-13} m^2. The error bar indicates the standard deviation of each sample if applicable.

brine salinity, and even the minimum vent VDF salinity is still greater than the bottom vapor salinity, which suggests that the mixing processes play an important role in determining vent fluid salinities. It is not appropriate to assume that the vent fluid salinity is that of the fluid

nearthe top of the AMC. In addition, for both permeability values, as MaxTbot increases, both bottom brine salinity and vent BDF salinity increase, and both bottom vapor salinity and vent VDF salinity decrease, which is consistent with the phase equilibria. Also, both bottom fluid salinities and vent fluid salinities from the simulations with different permeabilities are similar in most cases, which may indicate that the permeability doesn't have a great effect on fluid salinity in the systems considered. Because of the robust increasing or decreasing trend of fluid salinity and the relatively small effect of permeability, it may be possible to deduce the bottom pressure and temperature conditions from the vent fluid salinity if a finer temporal and spatial scale models can be evaluated. The bottom pressure, temperature and salinity are critical for understanding quartz dissolution and precipitation above the magma chamber [e.g., *Steele-MacInnis et al., 2011*].

Heat output from the hydrothermal system is given by $H = A_u(h_u - h_d)M_z$, where A_u is discharge area, h is the enthalpy of the fluid, and $M_z = \rho_f u_z$ is the upward vertical mass flux at the seafloor where $z = 0$. We assume that these 2D simulations represent an along axis system, and that the vent field is ~50 m wide across the axis, based on the width of the ASC (Axial Summit Caldera) at EPR 9°44.8'-9°51.5'N (40-70m) [*Haymon et al.*, 1991]. The hydrothermal heat output measurements by *Ramondenc et al.* [2006] at EPR 9°50'N yield a total heat output of ~ 325±160 MW with ~ 42±21 MW coming from high-temperature vents along the 2 km segment of ridge, which results in a total heat flux of ~162±80 MW/km with ~21±10 MW/km coming from high-temperature vents along the ridge. Because the vent fluid temperature and the mass flux vary with time, we calculate the mean heat output over time and its standard deviation for simulations S1 through S8 to show how the heat flux changes in response to MaxTbot and the

permeability. For reasons discussed above, only the time after the plume reaches the seafloor is considered.

Figure 3.10 shows that heat output increases slightly with increasing MaxTbot as expected from the results shown in Figure 3.8. However, when permeability increases by an order of magnitude from 10^{-13} m^2 to 10^{-12} m^2, the heat output also increases by nearly a factor of 10. Because the vent fluid temperature is essentially independent of permeability (Figure 3.8), the increase in heat output results from the increased mass flux associated with the higher permeability simulation. Phase separation may not affect the heat output and vent fluid temperature very much when a homogeneous constant permeability is assumed. However, in a natural hydrothermal system, quartz dissolution and precipitation resulting from phase separation [*Steele-MacInnis et al., 2011*] may change the permeability significantly, which will affect the heat flux.

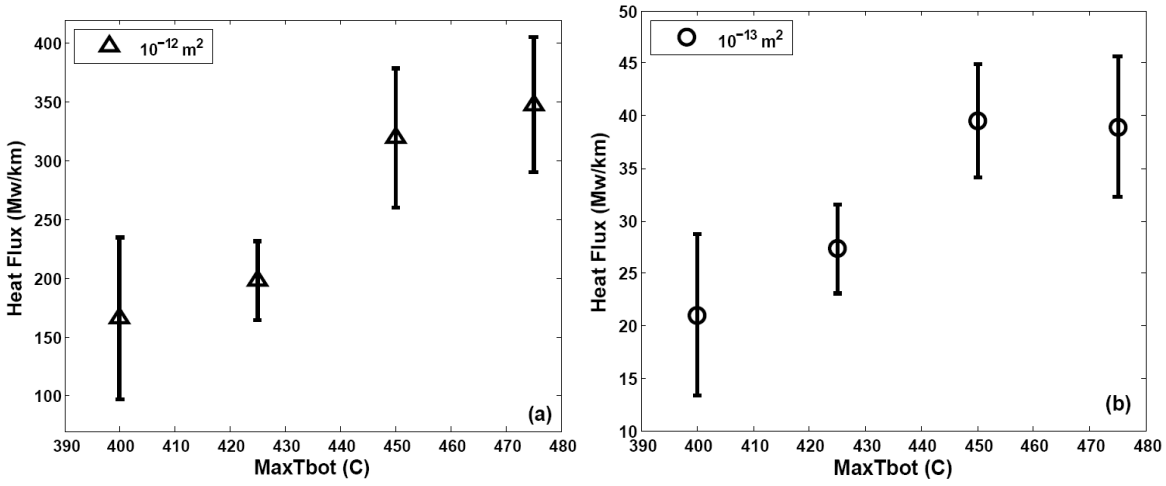

Figure 3.10 Seafloor heat flux as a function of MaxTbot at a seafloor pressure of 25 MPa and a system depth of 1km. Symbols show mean heat flux of different permeabilities: the triangle refers to 10^{-12} m^2, and the circle is 10^{-13} m^2. The error bars indicate the standard deviation of each sample. Note the different scale of y axis in the plots.

Although vent fluid features vary with time significantly, the quasi-steady state plume structures are relatively stable. Here we also investigate the effects of permeability by comparing

the detailed quasi-steady state plume structures of S1, S6 and S9. Figure 3.11 shows that for a given seafloor pressure, MaxTbot, and system depth, higher permeability results in more numerous and narrower plumes, and that plume structure becomes more complex [e.g., *Coumou et al.*, 2008]. Also the higher the permeability, the less time it takes for plumes to reach the seafloor and stabilize, and hence the shorter the simulation time needed to obtain quasi-steady state results. For example, it takes ~1 year for the simulation with permeability of 10^{-12} m^2, ~10 years for the simulation with permeability of 10^{-13} m^2 and ~100 years for the simulation with permeability of 10^{-14} m^2.

In the simulation with a homogeneous permeability of 10^{-13} m^2, the maximum vertical component of the Darcy velocity is ~2×10^{-6} m/s, so the actual velocity is ~2×10^{-5} m/s given that the porosity is assumed as 10% in the model. If the hydrothermal system is 1 km deep, then it will take the fluid at least ~5×10^{7} s (~1.5 years) to arrive at the seafloor from the bottom of the system where phase separation occurs. If the permeability of the system is 10^{-12} m^2, then the actual fluid velocity will be 1 order of magnitude higher (~2×10^{-4} m/s), and it will take 2 months for the fluid to travel from the bottom of the system to the seafloor. These velocities and time scales place limits on how long it might take for perturbations at the base of the system resulting from seismicity or magma replenishment to be evidenced at the seafloor.

In S1 with a homogeneous permeability of 10^{-13} m^2, it takes 10 years for the hot fluid (vapor or brine phase, >300 °C) to vent at the seafloor and 7 years for the VDF to reach the seafloor. However, if there is already a plume or travel path, it takes a much shorter time for the VDF to arrive at the seafloor. For example, if we run S1* from single phase mature result, and then increase the bottom temperature gradually to conditions in the two phase regime at that pressure, which has the same boundary conditions as S1 with a permeability of 10^{-13} m^2, it only

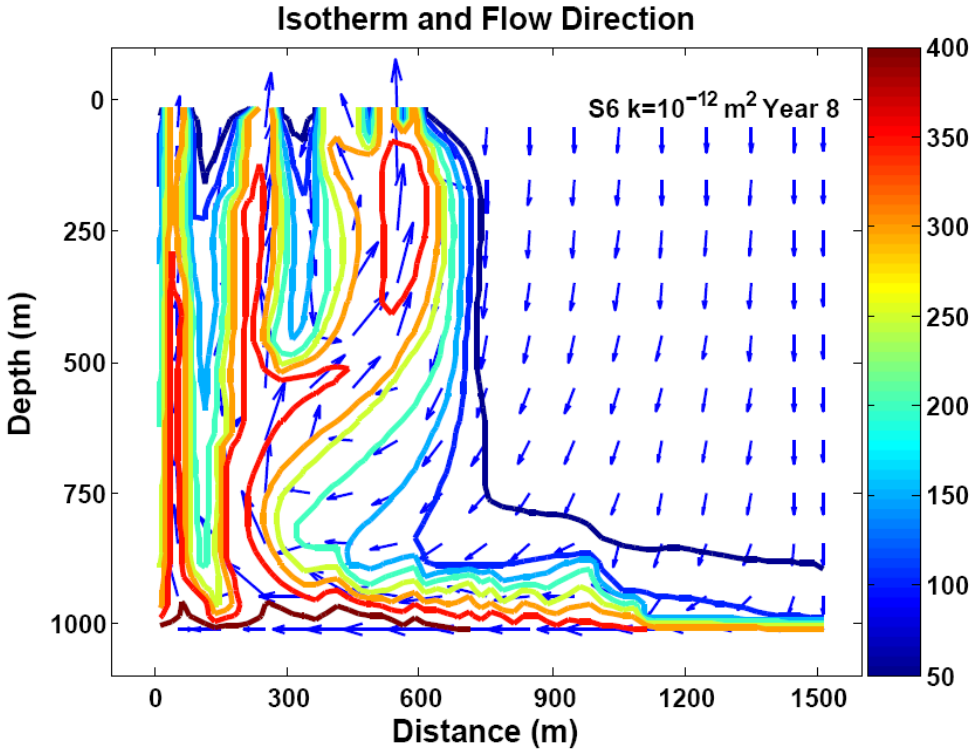
Isotherm and Flow Direction
S6 k=10^-12 m^2 Year 8
Depth (m)
Distance (m)
0
250
500
750
1000
0
300
600
900
1200
1500
400
350
300
250
200
150
100
50

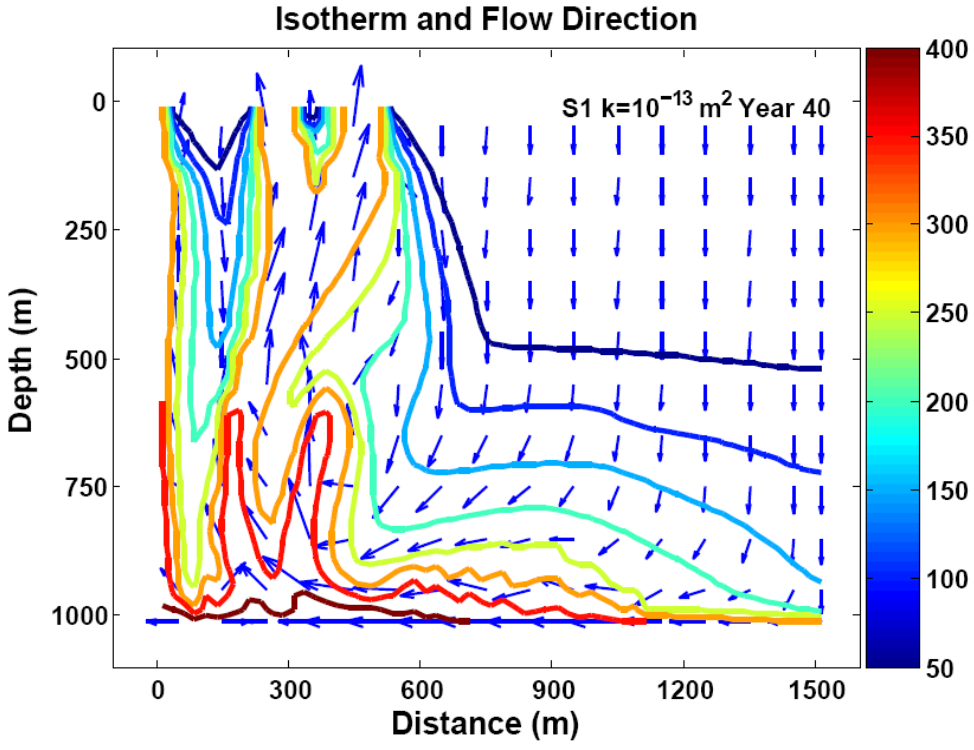
Isotherm and Flow Direction
S1 k=10^-13 m^2 Year 40
Depth (m)
Distance (m)
0
250
500
750
1000
0
300
600
900
1200
1500
400
350
300
250
200
150
100
50

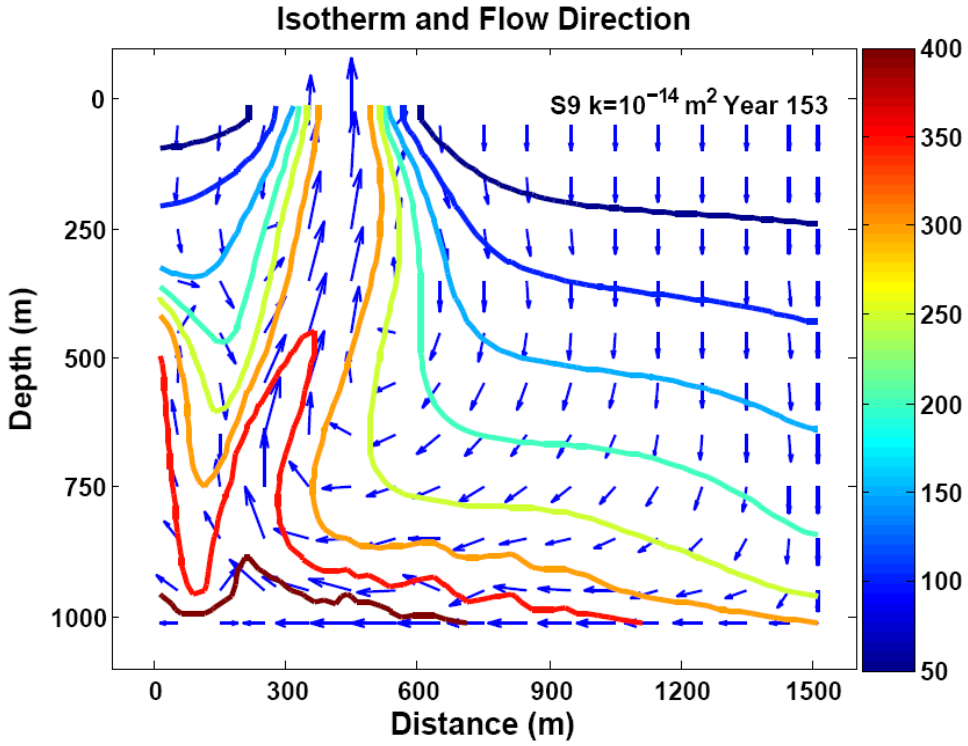

Figure 3.11 Quasi-steady state plume structures of simulation S1, S6 and S9 with different permeabilities. At the top is simulation S6 with a permeability of 10^{-12} m^2, in the middle is simulation S1 with a permeability of 10^{-13} m^2, and at the bottom is simulation S9 with a permeability of 10^{-14} m^2. Flow vectors have been re-gridded and rescaled in order to show the flow direction clearly, so they only represent relative magnitude instead of actual velocity. Plumes get denser and narrower or exhibit complex structure at mature state for higher permeabilities.

takes ~1.5 year for the VDF to travel from the bottom to the seafloor.

To further show the effect of permeability on two-phase hydrothermal flow, Figure 3.12 plots vent fluid temperature and salinity as a function of time for S1 and S9, in addition to that of S6 in Figure 3.4. Figure 3.4 and Figure 3.12 shows that vent fluid temperature and salinity range are essentially independent of the permeability, though it takes much longer for the lower permeability system (10^{-14} m^2) to reach equilibrium. Moreover, oscillations in vent fluid temperature and salinity become more frequent as the permeability increases. Both the time to achieve equilibrium and the frequency of oscillations in vent fluid temperature and salinity reflect the effects of permeability on *Ra*.

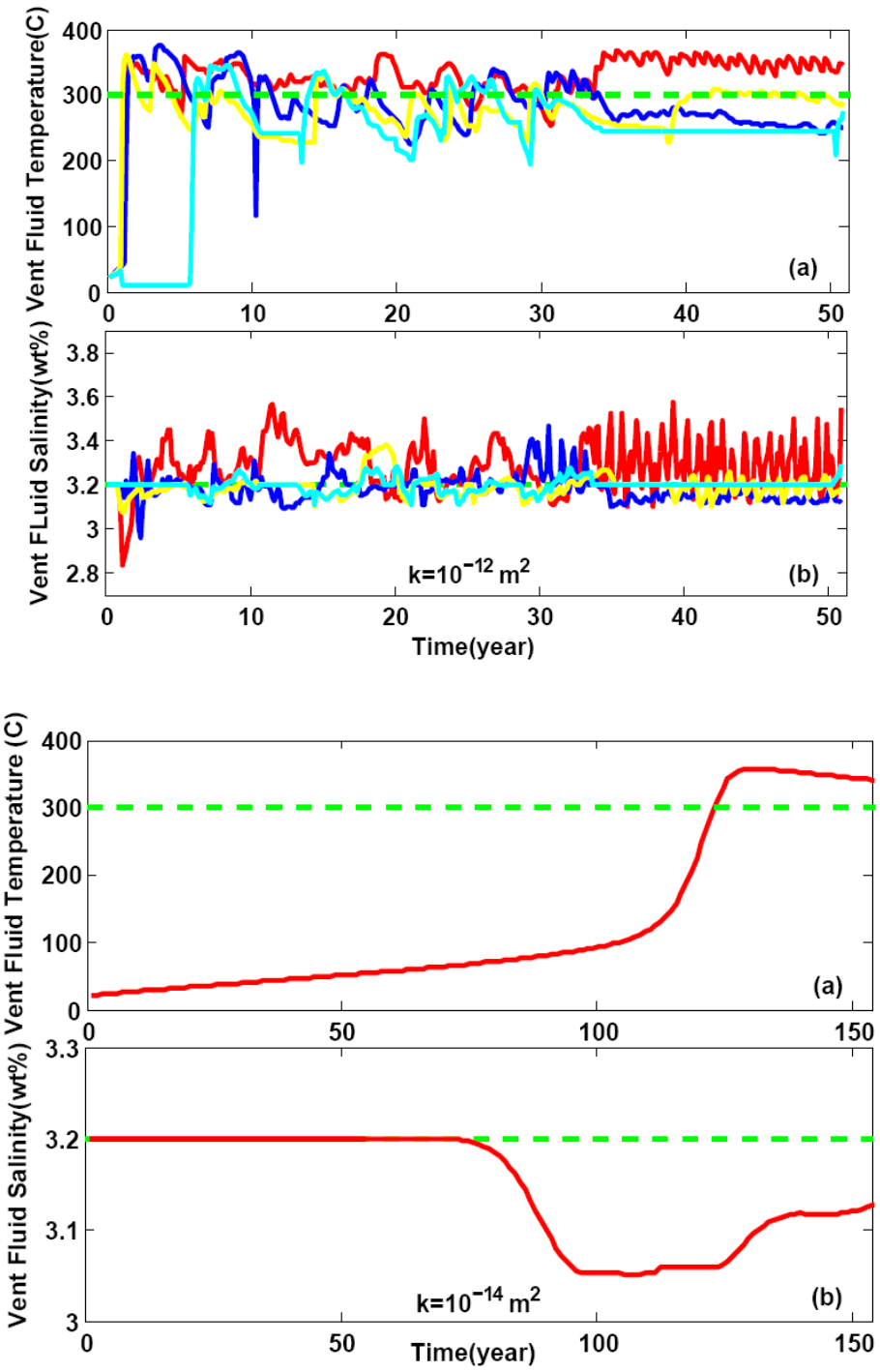

Figure 3.12 Vent fluid temperature and salinity evolution with time in different plumes for simulations S6 and S9, compared to that of S1 in Figure 3.4. At the top is the result of S6 with a permeability of 10^{-12} m^2, and at the bottom is that of S9 with a permeability of 10^{-14} m^2. Different colors show the results of different plumes. Red is the left-most plume, blue is the second one from the left, yellow is the third, and cyan is the fourth. Green dash lines show temperature of 300 °C and salinity of 3.2 wt%. The higher permeability system has more frequent variations.

In Figure 3.12, the first plume always evolves at the edge of the simulated AMC (500 m on the right from the center), where the bottom temperature increases to MaxTbot. The location of the first plume likely results from this sharp change of temperature gradient. The time when the plume reaches the seafloor indicates how long it will take for the high temperature fluid or low salinity seawater to arrive at the seafloor from the bottom of the hydrothermal system. The early fluid with a salinity differing from that of normal seawater venting at the seafloor is always the VDF due to its low density, and the higher density brine from phase separation initially remains at the bottom. After the brine layer accumulates for some time, it may break down and lead to BDF venting at the seafloor.

3.3.3 Spatial variation in vent fluid salinity

In some of the two phase simulations, both VDF and BDF could vent simultaneously from different plumes at the seafloor. This is shown in part in Figures 3.4 and 3.12. For example, in Figure 3.4 at year 50, the vent fluid salinity of the red plume is above that of seawater, while the vent fluid salinities of the yellow plume and the blue plume are below that of seawater. Even in a single broad temperature plume, VDF and BDF could vent simultaneously at different locations. This is common in all our two phase simulations. The salinity difference between vent VDF and BDF is up to 0.7 wt% even though they are from adjacent nodes in the model. This difference suggests incomplete mixing as a result of the mainly vertical flow direction of both VDF and BDF as they rise from different locations near the bottom of the system.

Figure 3.13 shows the temporal evolution of VDF and BDF flow in the whole system for S3. Initially, VDF vents to the seafloor and a brine layer forms at the bottom. As time goes on, the brine layer breaks down so that BDF vents from the central plume while the plume at the right still vents VDF as normal seawater flows from right to left at the bottom to produce more

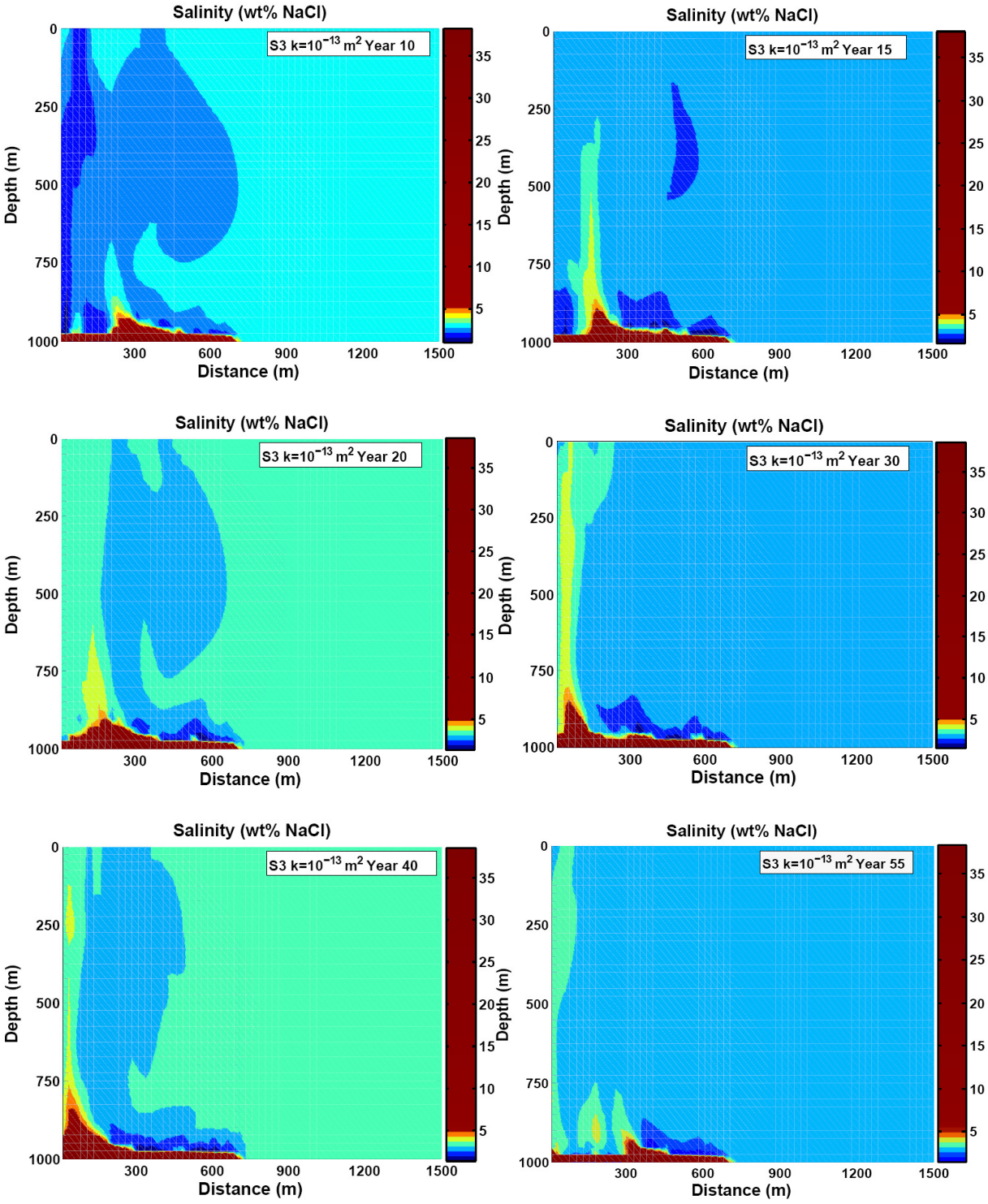

Figure 3.13 Evolution of VDF and BDF flow paths with time for simulation S3 in Table 3.1. Salinity color bar is scaled to make VDF and BDF easier to recognize.

vapor at the right side above magma chamber. In addition, VDF and BDF with a salinity difference of ~0.2 wt% could vent simultaneously at different locations from a single temperature plume at a distance of 250 m from the left side at year 22. The vent VDF and BDF salinity difference between different plumes could be higher (~1.0 wt%). Both VDF and BDF appear to rise through a channel in the plume. As time goes on, the channel of VDF could change to that of BDF, and vice versa.

3.3.4 Temporal variation in vent fluid temperature and salinity

The temporal variations of the vent fluid temperature and salinity are not simply periodic, which is consistent with high frequency measurements of vent fluid salinity and temperature in Juan de Fuca Ridge (Larson et al., 2007). They may be caused by the delayed response at the seafloor to physical conditions near the bottom even though the boundary condition at the bottom is unchanged. When the plume is hot at the seafloor, it facilitates the down-going fluid flow in the recharge zone adjacent to the plume which will cool the bottom part of the plume. Even though the plume at depth is cooled, the upper part of the thermal plume is still hot enough to support vent fluid temperature for a period of time. When the seafloor vent fluid cools, it slows down the recharging cold seawater, but it takes several years for a system with a permeability of 10^{-13} m^2 to heat the whole plume from the bottom to make the vent fluid hot again. As a result, vent fluid temperature will vary within a certain range, whereas the frequency of oscillation is controlled by the fluid flow velocity in the discharge and recharge zones, which are functions of the permeability. Vent fluid salinity variation is also affected by this cycle, but brine layer formation and destruction may also contribute to this variation.

3.4 Application for EPR 9°50′ N

Fluids from both Bio9 and P vent at EPR 9°50´ N have chloride concentrations that are different from seawater, suggesting that sub-seafloor phase separation has occurred. Although Bio9 and P vent are only ~60 m apart (*Von Damm,* 2004), repeated sampling of the vent fluids shows that their chlorinities evolve differently with time, with P vent reaching a chlorinity greater than seawater, while Bio 9 vent has remained less than seawater [upper left panel of Figure 3.1]. *Sohn et al.* [1998] and *Von Damm et al.* [2004] suggest that the two vents have different source regions or are driven by locally different heat sources. However, our simulation results in section 3.3.3 provide a different explanation.

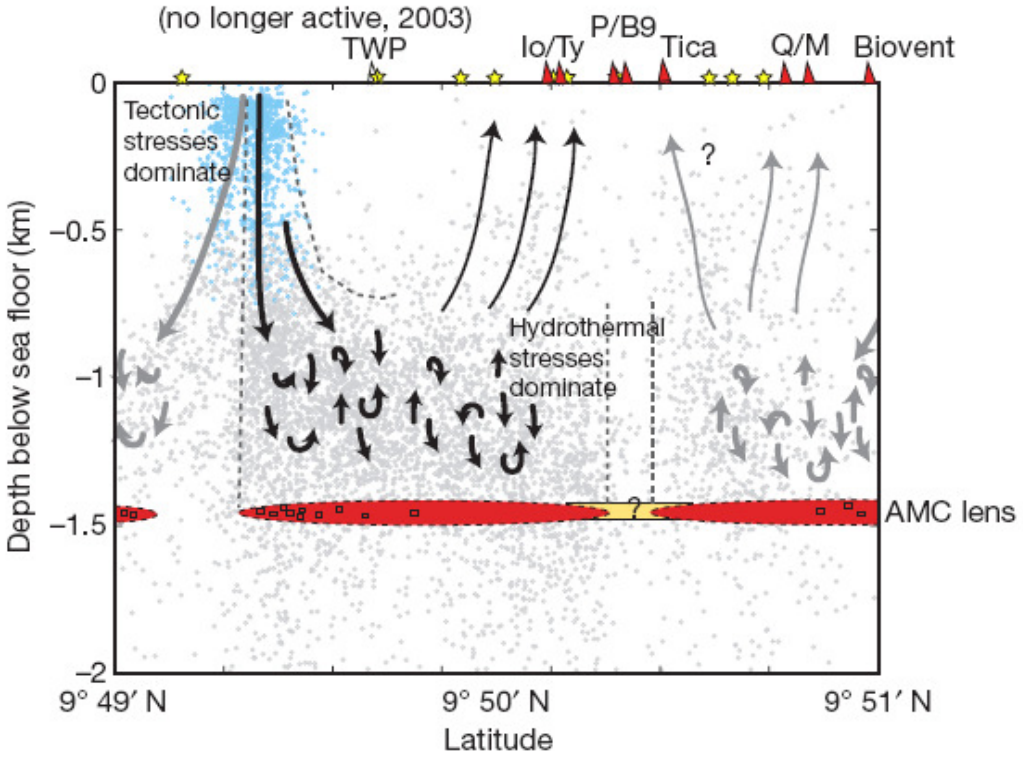

Figure 3.14 Hydrothermal cell structure model in the along axis direction proposed by *Tolstoy et al.* [2008] from exploration seismology and micro earthquake data. The features of the best-defined hydrothermal cell are shown with black arrows, and the features inferred in adjacent cells are shown with grey arrows. Light blue dots illustrate the area where tectonic stresses are likely to dominate earthquake generation, creating a zone of high permeability. Light grey dots illustrate where hydrothermal stresses probably dominate. The exact location of this transition is not well constrained.

As the hydrothermal cell structure model (Figure 3.14) proposed by *Tolstoy et al.* [2008] suggests, the axial magma chamber (AMC) lens along axis beneath P vent and Bio9 vent is about 1500 m long and 1500 m below the seafloor. The active high and low temperature hydrothermal vents such as P, Bio 9 and Ty/Io are distributed over about a 600 m region along the ridge axis. A simulation with a seafloor pressure of 25 MPa, MaxTbot of 450 °C, a permeability of 10^{-13} m^2, a system depth of 1.5 km, and a magma chamber half width of 500 m is used to study the vent field at EPR 9°50′ N. This simulation is taken as an example to discuss multiple plumes at the seafloor exhibiting salinity differences between plumes, or vent fluid temperature and salinity variation in a single given plume. The results are shown in Figure 3.15 and 3.16.

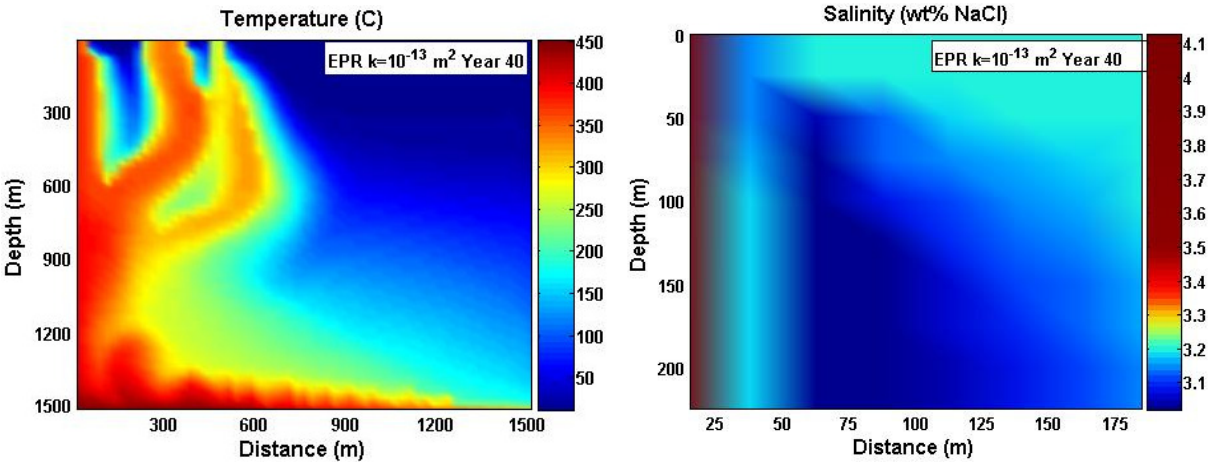

Figure 3.15 Temperature plumes and near surface salinity profile in the left-most plume of the simulation for EPR 9°50′ N at year 40. Three temperature plumes vent in a 600m region; BDF with salinity of 3.85 wt% and VDF with salinity of 3.15 wt% are venting simultaneously beside each other.

Figure 3.15 shows that 3 plumes with different vent fluid temperatures occur within a 600 m region at the seafloor at year 40, which is consistent with the multiple vents at EPR 9°50′ N. In the left-most plume, a BDF with a salinity of 3.85 wt% and a VDF with a salinity of 3.15 wt% vent simultaneously side by side, which could explain the observation that both VDF and BDF

with a salinity difference of ~0.7 wt% vented simultaneously in Bio 9 and P vent (~60 m apart) at EPR 9°50´ N.

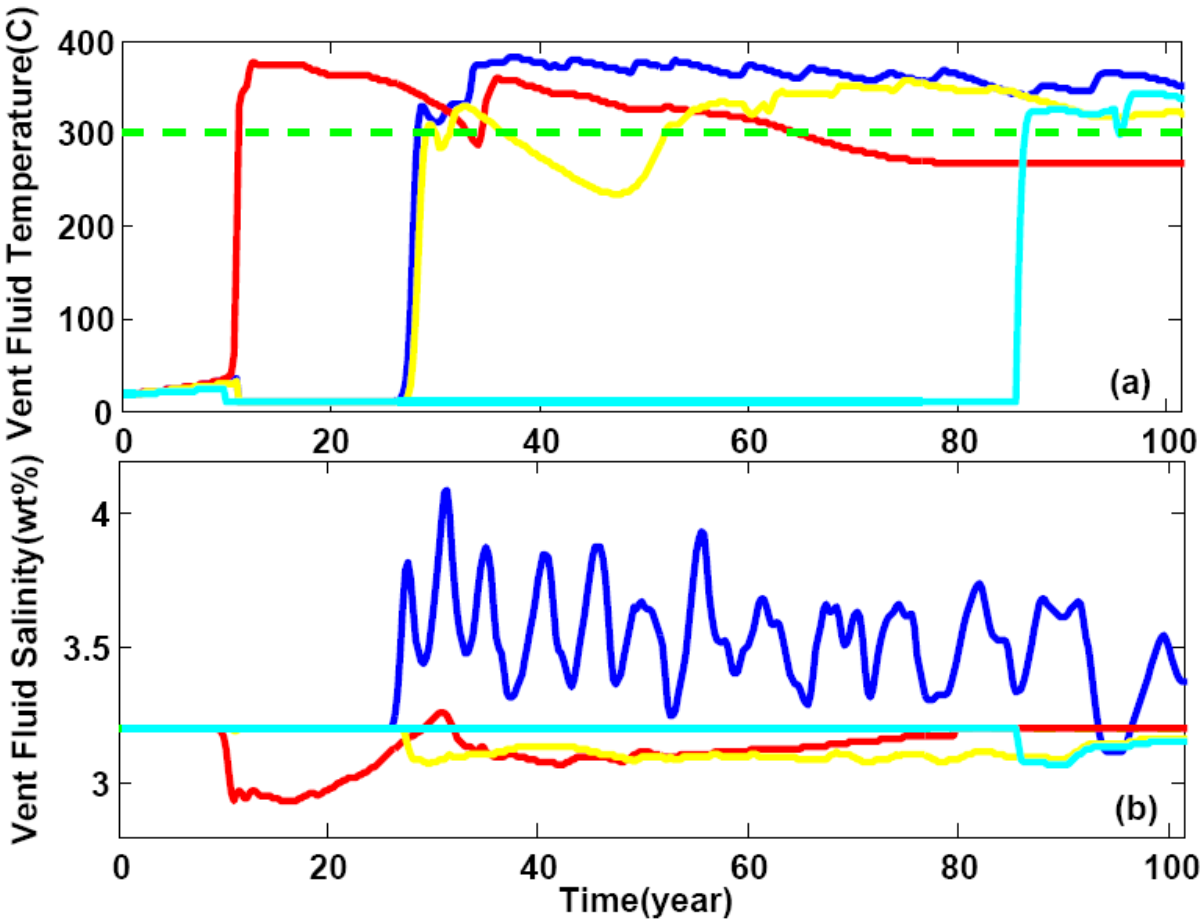

Figure 3.16 Vent fluid temperature and salinity evolution with time in different plumes of the simulation for EPR 9°50′N. Different colors show the results of different plumes. Red is the left-most plume, and blue is the second one from the left, yellow is the third one, and cyan is the fourth one. Green dash lines show temperature of 300 °C and salinity of 3.2 wt%. Note the latter plume occurs after the 40 year simulation time shown in Figure 3.15.

Figure 3.16 shows vent fluid temperature and salinity evolution with time in different plumes of the simulation for EPR 9°50′ N. VDF and BDF vent simultaneously at the seafloor from different plumes, even though the bottom boundary condition is identical. The variation pattern and frequency of the vent fluid temperature in the simulation is similar to that of

measurements by *Fornari et al.* [1998] and *Scheirer et al.* [2006] (Figure 3.17), but the maximum vent fluid temperature (~382 °C) and the mean vent fluid temperature (~362 °C) of the simulation are slightly colder than the EPR measurements.

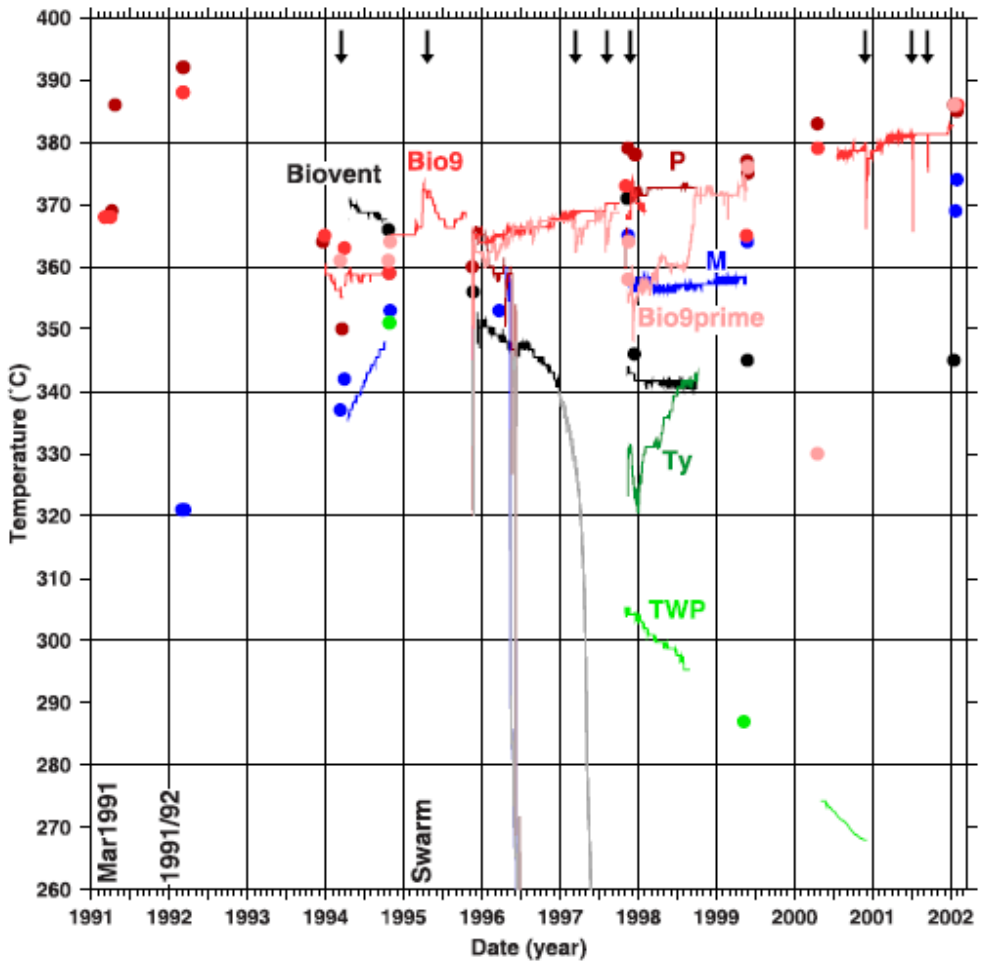

Figure 3.17 Vent fluid temperature variations between 1991 and 2002 at Bio9, P, Ty, TWP, Biovent and M vents. Discrete measurements made while sampling fluids from these vents are shown as dots [*Von Damm*, 1995, 2000]; continuous measurements with HOBO probes are shown as colored lines. Gray lines indicate when the continuous records reflect temperatures associated with vent sealing, chimney toppling, or other causes not related to changes in the vent effluent. Arrows indicate times of temperature excursions of one or more of the vents. [From *Scheirer et al.,* 2006]

3.5 Conclusions

The two phase simulation results presented here reproduce several features that have been observed in natural submarine hydrothermal systems. Multiple vents at the seafloor can overly a 500 m-wide simulated sub-axial magma chamber for different system depths and permeability of 10^{-13} m^2 and 10^{-12} m^2. The range in vent fluid temperature and salinity with time is a function of the boundary conditions. High salinity BDF and low salinity VDF could vent at the seafloor simultaneously, even from neighboring locations that are fed by the same plume. In addition, we find:

1) Bottom temperature has a greater effect on vent fluid temperature than permeability, but the temporal variability of vent fluid temperature suggests that subsurface permeability or bottom temperature cannot be deduced from vent fluid temperature alone.

2) Temporal variation can be due entirely to plume dynamics, and do not necessarily indicate changes at the AMC. Vent fluid salinity is strongly affected by mixing as the plume rises, therefore it does not necessarily directly reflect depth of the hydrothermal cell or the pressure and temperature conditions at which phase separation occurs.

3) Keeping other system parameters the same, higher permeability results in more abundant and narrower plumes, while lower permeability produces fewer but broader plumes. High permeability systems also evolve faster, provide higher heat flux, and undergo more rapid temporal variations.

4) The results of the simulation specific to EPR 9°50´ N are generally consistent with field observations, including multiple vents, vent fluid temperatures, and temporal and spatial variations in vent fluid salinity. In addition, the simultaneous venting of VDF and BDF from Bio9 and P vent is consistent with results of the simulation.

CHAPTER 4: RECOMMENDATIONS FOR FUTURE WORK

Although a number of simulations have been run in this thesis to understand phase separation in seafloor hydrothermal systems, the parameter space considered has been somewhat limited. In addition, other aspects of seafloor hydrothermal activity such as water-rock chemical reactions and the evolution of permeability, and coupling between hydrothermal and magmatic/tectonic activity have yet to be explored in any detail. Moreover, some real hydrothermal systems are likely to be 3-D rather than 2-D. Below is a list of several possible important research topics that can be worked on as an extension of this thesis.

4.1 Broader range of model parameters

The current work focused on surface pressure of 25 MPa and maximum bottom temperature of 400-500°C. Compared to CSMP++ [*Geiger et al.,* 2006a, 2006b; *Matthäi et al.,* 2007; *Coumou,* 2008; *Coumou et al.,* 2009], which also simulates multi-phase hydrothermal flow in NaCl-H_2O fluids, different surface pressures (15 MPa and 35 MPa) and higher bottom temperature (>500 °C) need to be explored using FISHES. Simulations with different permeability structure and bottom temperature/heat flux distribution may also be meaningful for understanding hydrothermal system. In addition, magma-hydrothermal systems in which the AMC lies at greater depths such as Lucky Strike [*Singh et al*., 2006] and systems with smaller or larger permeability need further study.

4.2 Feedback of geochemical reaction on permeability

The models in this thesis assume constant homogeneous permeability and porosity structure for simplicity. However, permeability and porosity likely to be highly heterogeneous and it may change as a result of geochemical reactions (e.g. quartz and anhydrite dissolution and precipitation). A temporally and spatially changing permeability structure may substantially alter fluid flow paths and heat transfer that may in turn yield different results than found with constant, homogeneous permeability. For example, preliminary modeling of quartz dissolution and precipitation in the presence of two-phase flow suggest that mineral precipitation near the bottom of the system could decrease permeability hence preserve more high salinity brine [*MacInnis et al.*, 2011]. Permeability changes near a buoyant plume may affect the heat output at the seafloor by changing fluid velocity, flow pattern and mass flux. New permeability distributions near the seafloor may produce different vent areas. In turn, all these changes in fluid flow and fluid properties may exert feedbacks on the permeability and porosity of system itself leading to a continually evolving system.

4.3 Coupling of seafloor hydrothermal system with magmatic and tectonic processes and events

Seafloor hydrothermal systems are supported by the heat output from the magma chamber beneath it. *Liu and Lowell* (2009) developed a model to calculate the heat output with time from a magma chamber that differs in magma replenishment rate, the type of magma and crystal distribution in the magma chamber. Current models assume constant temperature or constant heat flux at the bottom of seafloor hydrothermal system, which is somewhat idealistic. It would be useful to couple a seafloor hydrothermal system with models of magma convection and replenishment, in order to better understand these interconnected processes. In particular, it

would be useful to understand the evolution of the two-phase hydrothermal system after a diking event.

4.4 3-D two phase numerical modeling of seafloor hydrothermal systems

In this thesis, 2-D numerical simulations were used as a result of limited computer resources, and because FISHES has not yet been constructed for 3-D simulations. Natural hydrothermal systems are likely to be three dimensional, however. Three-dimensional modeling may be necessary to explain observations such as, the trend of decreasing vent fluid salinity and increasing vent temperature from north to south at Main Endeavor Field, Juan de Fuca Ridge. Moreover, 2-D models cannot determine the three-dimensional plume shape in a homogeneous permeability medium. This feature was highlighted in *Coumou et al.* [2008] where three dimensional simulations in a single-phase system were performed.

REFERENCES

Anderko, A., and K. Pitzer (1993), Equation-of-state representation of phase equilibria and volumetric properties of the system NaCl-H_2O above 573K, *Geochim. Cosmochim. Acta*, 57, 1657-1680.

Archer, D. (1992), Thermodynamic properties of the NaCl+H2O system II. Thermodynamic properties of NaCl (aq), NaCl·$2H_2O$ (cr), and phase equilibria, *J. Phys. Chem. Ref. Data, 21,* 793-820.

Bai, W., W. Xu, and R. P. Lowell (2003), The dynamics of submarine geothermal heat pipes, *Geophys. Res. Lett., 30*(3), 1108, doi:10.1029/2002GL016176.

Berndt, M. E., and W. E. Seyfried, Jr. (1990), Boron, bromine, and other trace elements as clues to the fate of chlorine in mid-ocean ridge vent fluids*, Geochim. Cosmochim. Acta, 54,* 2235-2245.

Bischoff, J. L., and K. S. Pitzer (1989), Liquid-vapor relations for the system NaCl-H_2O: Summary of the P-T-x surface from 300° to 500°C, *Am. J. Sci., 289*, 217-248.

Bischoff, J., and R. Rosenbauer (1984), The critical point and two-phase boundary of seawater, 200° - 500 °C, *Earth Planet. Sci. Lett., 68*, 172-180.

Bodvarsson, G., and R. P. Lowell (1972), Ocean-floor heat flow and the circulation of interstitial waters, *J. Geophys. Res., 77*, 4472-4475.

Bower, K. M., and G. Zyvoloski (1997), A numerical model for thermo-hydro-mechanical coupling in fractured rock, *Int. J. Rock Mech. Min. Sci., 34*, 1201-1211.

Brikowski, T., and D. Norton (1989), Influence of magma chamber geometry on hydrothermal activity at mid-ocean ridges, *Earth Planet. Sci. Lett., 93*, 241-255.

Buck, W. R., P. T. Delaney, J. A. Karson, and Y. Lagabrielle, editors, (1998), *Faulting and magmatism at mid-ocean ridges, Geophys. Monogr. Ser., v. 106,* 348 pp., American Geophys. Union, Washington, D. C.

Butterfield, D. A., R. E. McDuff, M. J. Mottl, M. D. Lilley, J. E. Lupton, and G. J. Massoth (1994), Gradients in the composition of hydrothermal fluids from the Endeavour segment vent field: Phase separation and brine loss, *J. Geophys. Res., 99,* 9561-9583.

Cathles, L. M. (1977), An analysis of the cooling of intrusive by ground-water convection which includes boiling, *Econ. Geol., 72*, 804-826.

Coumou, D., T. Driesner, S. Geiger, C. A. Heinrich, and S. Matthäi (2006), The dynamics of mid-ocean ridge hydrothermal systems: Splitting plumes and fluctuating vent temperatures, *Earth Planet. Sci. Lett., 245*, 218-235.

Coumou, D. (2008), Numerical simulation of fluid flow in mid-ocean ridge hydrothermal systems, Ph.D. thesis, ETH Zurich, Zurich, Switzerland.

Coumou, D., T. Driesner, and C. Heinrich (2008a), Heat transport at boiling, near-critical conditions, *Geofluids, 8*, 208-215.

Coumou, D., T. Driesner, and C. Heinrich (2008b), The structure and dynamics of mid-ocean ridge hydrothermal systems, *Science, 321*, 1825-1828.

Coumou, D., T. Driesner, P. Weis, and C. Heinrich (2009), Phase separation, brine formation, and salinity variation at Black Smoker hydrothermal systems, *J. Geophys. Res., 114*, B03212, doi:10.1029/2008JB005764.

Detrick, R. S., P. Buhl, E. Vera, J. Mutter, J. Orcutt, J. Madsen, and T. Brocher (1987), Multi-channel seismic imaging of a crustal magma chamber along the East Pacific Rise, *Nature, 326*, 35-41.

Driesner, T., and C. Heinrich (2007), The system H2O-NaCl. Part I: Correlation formulae for phase relations in temperature-pressure-compositions pace from 0 to 1000 °C, 0 to 5000 bar, and 0 to 1 X_{NaCl}, *Geochim. Cosmochim. Acta, 71*, 4880-4901.

Elder, J. W. (1965), Physical processes in geothermal areas, in *Terrestrial Heat Flow, Geophys. Monogr. Ser.,* vol. 8, edited by W. H. K. Lee, pp. 211-239, AGU, Washington, D. C.

Elder, J. (1967), Transient convection in a porous medium, *J. Fluid Mech., 27*, 609-623.

Faust, C. R., and J. W. Mercer (1979), Geothermal reservoir simulation: 1. Mathematical models for liquid- and vapor-dominated hydrothermal systems, *Water Resour. Res., 15*, 23-30.

Fehn, U., and L. Cathles (1979), Hydrothermal convection at slow-spreading midocean ridges, *Tectonophysics, 55,* 239-260.

Fehn, U., and L. Cathles (1986), The influence of plate movement on the evolution of hydrothermal convection cells in the oceanic crust, *Tectonophysics, 125*, 289-312.

Fehn, U., K. E. Green, R. P. Von Herzen, and L. M. Cathles (1983), Numerical models for the hydrothermal field at the Galapagos Spreading Center, *J. Geophys. Res., 88*, 1033-1048.

Foutaine, F. J., and W. S. D. Wilcock (2007), Two-dimensional numerical models of open-top hydrothermal convection at high Rayleigh and Nusselt numbers: Implications for mid-ocean ridge hydrothermal circulation, *Geochem. Geophys. Geosyst., 8*, Q07010, doi:10.1029/2007GC001601.

Fontaine, F., W. Wilcock, and D. Butterfield (2007), Physical controls on the salinity of mid-ocean ridge hydrothermal vent fluids, *Earth Planet. Sci. Lett., 257*, 132-145

Fornari, D. J., K. L. Von Damm, T. K. P. Gregg, M. Lilley, G. Levai, A. Bray, R. M. Haymon, M. R. Perfit, and R. Lutz (1998b), Time-series temperature measurements at high-temperature hydrothermal vents, East Pacific Rise 9°49'-51'N: Evidence for monitoring a crustal cracking event, *Earth Planet. Sci. Lett., 160,* 419-431.

Geiger, S., T. Driesner, C. A. Heinrich, and S. K. Matthäi (2006a), Multiphase thermohaline convection in the Earth's crust: I. A new finite element-finite volume solution technique combined with a new equation of state for NaCl-H_2O, *Transp. Porous Media, 63*, 399-434.

Geiger, S., T. Driesner, C. A. Heinrich, and S. K. Matthäi (2006b), Multiphase thermohaline convection in the Earth's crust: II. Benchmarking and application of a finite element-finite volume solution technique with a NaCl-H_2O equation of state, *Transp. Porous Media, 63*, 435-461.

German, C. R., J. Lin, and L. M. Parson, editors, (2004), Mid-ocean ridges: Hydrothermal interactions between the lithosphere and oceans, *Geophys. Monogr. Ser., v. 148,* 318 pp., American Geophys. Union, Washington, D. C.

Haymon, R. M., D. J. Fornari, M. H. Edwards, S. Carbotte, D. Wright, and K. C. Macdonald (1991), Hydrothermal vent distribution along the East Pacific Rise crest (9°09'-54'N) and its relationship to magmatic and tectonic processes on fast-spreading mid-ocean ridges, *Earth Planet. Sci. Lett., 104*, 513-534.

Haymon, R. M., D. J. Fornari, K. L. Von Damm, M. D. Lilley, M. R. Perfit, J. M. Edmond, W. C. Shanks, III, R. A. Lutz, J. M. Grebmeier, S. Carbotte, D. Wright, E. McLaughlin, M. Smith, N. Beedle, and E. Olson (1993), Volcanic eruption of the mid-ocean ridge along the East Pacific Rise crest at 9°45'-52'N: Direct submersible observations of seafloor phenomena associated with an eruption even in April, 1991, *Earth Planet. Sci. Lett., 119*, 85-101.

Hannington, M. D., I. R. Jonasson, P. M. Herzig, and S. Petersen (1995), Physical and chemical processes of seaflorr mineralization at mid-ocean ridges, in *Seafloor Hydrothermal Systems: Physical, Chemical, Biological, and Geological Interactions, Geophys. Monogr. Ser.,* vol. 91, edited by S. E. Humphris, R. A. Zierenberg, L. S. Mullineaux, and R. E. Thomson, pp. 115-157, AGU, Washington, D. C.

Horton, E. W., and F. T. Rogers, Jr. (1945), Convection currents in porous media, *J. Appl. Phys., 16*, 367-370.

Ingebritsen, S. E., and D. O. Hayba (1994), Fluid flow and heat transport near the critical point of H_2O, *Geophys. Res. Lett., 21*, 2199-2203.

Humphris, S. E., R. A. Zierenberg, L. S. Mullineaux, and R. E. Thomson, editors, (1995), *Seafloor hydrothermal systems: Physical, chemical, biological, and geological interactions, Geophys. Monogr. Ser., v. 91,* 466 pp., American Geophys. Union, Washington, D. C.

Jupp, T., and A. Schultz (2000), A thermodynamic explanation for black smoker temperatures, *Nature, 403*, 880-883.

Kawada, Y., S. Yoshida, and S. I. Watanabe (2004), Numerical simulations of mid-ocean ridge hydrothermal circulation including the phase separation of seawater, *Earth Planets Space, 56*, 193-215.

Kelly, D. S., and J. R. Delaney (1987), Two-phase separation and fracturing in mid-ocean ridge gabbros at temperatures greater than 700 °C, *Earth Planet. Sci. Lett., 83*, 53-66.

Kissling, W. (2005a), Transport of three-phase hyper-saline brines in porous media: theory and code implementation, *Transp. Porous Media, 61*, 25-44.

Kissling, W. (2005b), Transport of three-phase hyper-saline brines in porous media: examples, *Transp. Porous Media, 60*, 141-157.

Lapwood, E., Convection of a fluid in a porous media, *Proc. Cambridge philos. Soc., 44*, 508-521.

Larson, B. I., E. J. Olson, and M. D. Lilley (2007), In situ measurement of dissolved chloride in high temperature hydrothermal fluids, *Geochim. Cosmochim. Acta, 71*, 2510-2523.

Lewis, K. C. (2007), Numerical modeling of two-phase flow in the sodium chloride-water system with applications to seafloor hydrothermal systems, Ph.D. thesis, Ga. Inst. of Technol., Atlanta.

Lewis, K. C., and R. P. Lowell (2004), Mathematical modeling of phase separation of seawater near an igneous dike*, Geofluids, 4*, 197-209.

Lewis, K. C., and R. P. Lowell (2009a), Numerical modeling of two-phase flow in the NaCl-H_2O system: Introduction of a numerical method and benchmarking*, J. Geophys. Res., 114*, B05202, doi:10.1029/2008JB006029.

Lewis, K. C., and R. P. Lowell (2009b), Numerical modeling of two-phase flow in the NaCl-H_2O system: 2. Examples*, J. Geophys. Res., 114*, B08204, doi:10.1029/2008JB006030.

Liu, L., and R. P. Lowell (2009), Models of hydrothermal heat output from a convecting, crystallizing, replenished magma chamber beneath an oceanic spreading center, *J. Geophys. Res., 114,* B02102, doi:10.1029/2008JB005846.

Lilley, M. D., D. A. Butterfield, J. E. Lupton, and E. J. Olson (2003), Magmatic events can produce rapid changes in hydrothermal vent chemistry, *Nature, 422,* 878-881.

Lister, C. R. B. (1972), On the thermal balance of a mid-ocean ridge, *Geophys. J. R. Astron. Soc., 26*, 515-535.

Lister, C. R. B. (1974), On the penetration of water into hot rock, *Geophys. J. R. Astron. Soc., 39,* 465-509.

Lowell, R. P. (1975), Circulation in fractures, hot springs, and convective heat transport on mid-ocean ridge crests, *Geophys. J. R. Astron. Soc., 40*, 351-365.

Lowell, R. P., and D. K. Burnell (1991), Mathematical modeling of conductive heat transfer from a freezing convecting magma chamber to a single-pass hydrothermal system: Implications for sea floor black smokers*, Earth Planet. Sci. Lett.*, *104*, 59-69.

Lowell, R. P., and L. N. Germanovich (1994), On the temporal evolution of high-temperature hydrothermal systems at ocean ridge crests, *J. Geophys. Res., 99*, 565-575.

Lowell, R. P., and L. N. Germanovich (2004), Hydrothermal processes at mid-ocean ridges: Results from scale analysis and single-pass models, in *Mid-Ocean Ridges: Hydrothermal Interactions Between the Lithosphere and Oceans, Geophys. Monogr.Ser.,* vol. 148, edited by C. German, J. Lin, and L. M. Parson, pp. 219-244, AGU, Washington, D. C.

Lowell, R. P., J. S. Seewald, A. Metaxas, and M. R. Perfit, editors, (2008), *Magma to microbe*: *Modeling hydrothermal processes at oceanic spreading centers*, *Geophys. Monogr. Ser.*, v. *178*, 285 pp., American Geophys. Union, Washington, D. C.

Lowell, R. P. and W. Xu (2000), Sub-critical two-phase seawater convection near a dike, *Earth Planet. Sci. Lett., 174*, 385-396.

Matthäi, S. K., et al. (2007), Numerical simulations of multiphase fluid flow in structurally complex reservoirs, in Structurally Complex Reservoir, edited by S. J. Jolley et al., *Geol. Soc. Spec. Publ., 292*, 405-429.

Mckenzie, D. P. (1965), Some remarks on heat flow and gravity anomalies, in *Terrestrial Heat Flow, Geophys. Monogr. Ser.,* vol. 8, edited by W. H. K. Lee, pp. 240-260, AGU, Washington, D. C.

Nehlig, P. (1991), Salinity of oceanic hydrothermal fluids: a fluid inclusion study, *Earth Planet. Sci. Lett., 102*, 310-325.

Nield, D. A. (1968), Onset of thermohaline convection in a porous medium, *Water Resour. Res., 1*, 553-560.

Palliser, C., and R. Mckibbin (1998a), A model for deep geothermal brines, I: T-p-X state-space description, *Transp. Porous Media, 33*, 65-80.

Palliser, C., and R. Mckibbin (1998b), A model for deep geothermal brines, II: Thermodynamic properties—Density, *Transp. Porous Media, 33*, 129-154.

Palliser, C., and R. Mckibbin (1998c), A model for deep geothermal brines, III: Thermaodynamic properties—Enthalpy and viscosity, *Transp. Porous Media, 33*, 155-171.

Parker, R. L., and D. W. Oldenburg (1973), Thermal model of ocean ridges, *Nature, Phys. Sci., 242*, 137-139.

Patankar, S. (1980*), Numerical Heat Transfer and Heat Flow,* Taylor and Francis, London.

Ramondenc, P., L. N. Germanovich, K. L. Von Damm, and R. P. Lowell (2006), The first measurements of hydrothermal heat output at 9°50'N, East Pacific Rise*, Earth Planet. Sci. Lett., 245*, 487-497.

Rona., P. A., C. W. Devey, J. Dyment, and B. J. Murton, editors, (2010), Diversity of hydrothermal systems on slow spreading ocean ridges, *Geophys. Monogr. Ser., v. 188,* 440 pp., American Geophys. Union, Washington, D. C.

Scheirer, D. S., T. M. Shank, and D. J. Fornari (2006), Temperature variations at diffuse and focused flow hydrothermal vent sites along the northern East Pacific Rise, *Geochem. Geophys. Geosyst.,7*, Q03002, doi:10.1029/2005GC001094.

Sclater, J. G., and J. Francheteau (1970), The implications of terrestrial heat-flow observations on current tectonic and geochemical models of the crust and upper mantle of the Earth, *Geophys. J. R. Astron. Soc., 20*, 509-542.

Sclater, J. G., C. Jaupart, and D. Galson (1980), The heat flow through the oceanic and continental crust and the heat loss of the Earth, *Rev. Geophys., 18*, 269-311.

Seyfried, W. E., Jr., M. E. Berndt, and D. R. Janecky (1986), Chloride depletions and enrichments in seafloor hydrothermal fluids: Constraints from experimental basalt alteration studies, *Geochim. Cosmochim. Acta, 50*, 469-475.

Seyfried, W. E., Jr., K. Ding, and M. E. Berndt (1991), Phase equilibria constraints on the chemistry of hot spring fluids at mid-ocean ridges, *Geochim. Cosmochim. Acta, 55*, 3559-3580.

Shank, T. M., D. J. Fornari, K. L. Von Damm, M. D. Lilley, R. M. Haymon, and R. A. Lutz (1998), Temporal and spatial patterns of biological community development at nascent deep-sea hydrothermal vents (9°50'N, East Pacific Rise), *Deep-Sea Research II, 45*, 465-515.

Singh, S. C., W. C. Crawford, H. Carton, T. Seher, V. Combier, M. Cannat, J. P. Canales, D. Düsünür, J. Escartin, and J. M. Miranda (2006), Discovery of a magma chamber and faults beneath a Mid-Atlantic Ridge hydrothermal field, *Nature, 332*, 1029-1032.

Sohn, R. A., D. J. Fornari, K. L. Von Damm, J. A. Hildebrand, and S. C. Webb (1998), Seismic and hydrothermal evidence for a cracking even on the East Pacific Rise crest at 9°50'N, *Nature, 396*,159-161.

Spiess, F. N., K. C. Macdonald, T. Atwater, R. Ballard, A. Carranza, D. Cordoba, C. Cox, V. M. Diaz Garcia, J. Francheteau, J. Guerrero, J. Hawkins, R. Haymon, R. Hessler, T. Juteau, M. Kastner, R. Larson, B. Luyendyk, J. D. Macdougall, S. Miller, W. Normark, J. Orcutt, and C. Rangin (1980), East Pacific Rise: Hot springs and geophysical experiments, *Science, 207*, 1421-1433.

Steele-MacInnis, M., L. Han, R. P. Lowell, J. D. Rimstidt, and R. J. Bodnar (2011), The role of fluid phase immiscibility in quartz dissolution and precipitation in sub-seafloor hydrothermal systems, *Earth Planet. Sci. Lett.,* in review.

Strens, M. R., and J. R. Cann (1982), A model of hydrothermal circulation in fault zones at mid-ocean ridge crests, *Geophys. J. R. Astron. Soc., 71*, 225-240.

Tanger, J., and K. Pitzer (1989), Thermodynamics of NaCl-H_2O: A new equation of state for the near-critical region and comparisons with other equations for adjoining regions, *Geochim. Cosmochim. Acta, 53*, 973-987.

Tolstoy, M., F. Waldhauser, D. R. Bohnenstiehl, R. T. Weekly and W. -Y. Kim (2008), Seismic identification of along-axis hydrothermal flow on the East Pacific Rise, *Nature, 451*, 181-184.

Von Damm, K. L. (1995), Controls on the chemistry and temporal variability of seafloor hydrothermal fluids, in *Seafloor Hydrothermal Systems, Geophys. Monogr. Ser., vol 91,* edited by S. E. Humphris, R. A. Zierenberg, L. S. Mullineaux, R. E. Thomson, pp. 222-247, AGU, Washington, D. C.

Von Damm, K. L. (2000), Chemistry of hydrothermal vent fluids from 9°-10°N, East Pacific Rise: "Time zero", the intermediate posteruptive period, *J. Geophys. Res., 105*, 11203-11222.

Von Damm, K. L. (2004), Evolution of the hydrothermal system at East Pacific Rise 9°50'N: Geochemical evidence for changes in the upper oceanic crust, in *Mid-Ocean Ridges: Hydrothermal Interactions Between the Lithosphere and Oceans, Geophys. Monogr. Ser.,* vol 148, edited by C. R. German, J. Lin, and L. M. Parson, pp. 285-304, AGU, Washington, D. C.

Von Damm, K. L., L. G. Buttermore, S. E. Oosting, A. M. Bray, D. J. Fornari, M. D. Lilley, and W. C. Shanks, III (1997), Direct observation of the evolution of a seafloor 'black smoker' from vapor to brine, *Earth Planet. Sci. Lett., 149*, 101-111.

Von Damm, K. L., C. M. Parker, R. M. Gallant, and J. P. Loveless (2002), Chemical evolution of hydrothermal fluids from EPR 21° N: 23 year later in a phase separating world, *Eos Trans. AGU, 83*(47), Fall Meet. Suppl., Abstract V61B-1365.

Von Damm, K. L., and M. D. Lilley (2004), Diffuse flow hydrothermal fluids from 9°50'N East Pacific Rise: Origin, evolution and biogeochemical controls, in *The Subseafloor Biosphere at Mid-Ocean Ridges, Geophys. Monogr. Ser.*, vol 144, edited by W. S. D. Wilcock, E. F. Delong, D. S. Kelley, J. A. Baross, and S. C. Cary, pp. 245-268, AGU, Wahsington, D. C.

Wilcock, W. S. D. (1998), Cellular convection models of mid-ocean ridge hydrothermal convection and the temperatures of black smoker fluids, *J. Geophys. Res., 103*, 2585-2596.

Wilcock, W. S. D., E. F. Delong, D. S. Kelley, J. A. Baross, and S. C. Cary, editors, (2004), The subseafloor biosphere at mid-ocean ridges, *Geophys. Monogr. Ser., v. 144,* 399 pp., American Geophys. Union, Washington, D. C.

William, D. L., and R. P. Von Herzen (1974), Heat loss from the Earth: New estimate, *Geology, 2*, 327-328.

Zyvoloski, G. A., Z. V. Dash, and S. Kelkar (1998), FEHM: Finite element heat and mass transfer code, *Rep. LA-11224-MS,* Los Alamos, Natl. Lab., Los Alamos, N. M.

Zyvoloski, G. A., B. A. Robinson, Z. D. Dash, and L. L. Trease (1997), Summary of models and methods for the FEHM application—A finite-element heat- and mass-transfer code, *Rep. LA-13307-MS,* Los Alamos, Natl. Lab., Los Alamos, N. M.

APPENDIX A: FORTRAN AND MATLAB CODE

A FORTRAN program is written to pick necessary information from output of FISHES, in order to calculate heat flux, mass flux and to analyze vent fluid temperature and salinity. The code is as below.

```
program HeatSaltflux

implicit none
real ::
Times(1000),Rho(400),VelverV(200),VelverL(200),Entha(200),Temp(200),Sali(11000),extr_sal
i(2)
character :: Label(15),c1*100
integer :: i,k,m,n,J,EOF,Counter,Flag

open(unit=10,file='OutFile1',status='old')
open(unit=11,file='OutFile2',status='old')
open(unit=12,file='Times.dat')
open(unit=13,file='Density1.dat')
open(unit=14,file='Density2.dat')
open(unit=15,file='Enthalpy.dat')
open(unit=16,file='VelVL.dat')
open(unit=17,file='VelVV.dat')
open(unit=18,file='Temperature.dat')
open(unit=19,file='Surf_Sali.dat')
open(unit=20,file='Extreme_Sali.dat')

write(*,*) 'Input Number of columns'
read(*,*) n
write(*,*) 'Input Number of rows'
read(*,*) m

15 format(1000E14.7) ! Liquid Volume Saturations,Temperature,Densities
10 format(5A)
11 format(1x,5A)
20 format(T27,E20.15)
30 format(T6,5A)
35 format(5x,13A)
36 format(100a)
40 format(1000E12.5) !Salinities
50 format(1000E16.8) ! Enthalpies,Velocities
```

```
Counter = 1
EOF = 0

9997   read(10,10,end=9998) (Label(J),J=1,5)
  if ((Label(1)=='P').and.(Label(5)=='t')) then
    backspace(10)
    read(10,20) Times(Counter)
    write(12,*) Times(Counter)
    Flag = 0
    do while (Flag==0)
      read(10,30) (Label(J),J=1,5)
      if ((Label(1)=='D').and.(Label(5)=='i')) then
        Flag = 1
      end if
    end do
    read(10,*)
    read(10,*)
    read(10,*) (Rho(J),J=1,2*n)

    Flag=0
    do while (Flag==0)
      read(10,30) (Label(J),J=1,5)
      if ((Label(1)=='T').and.(Label(5)=='e')) then
        Flag = 1
      end if
    end do
    read(10,*)
    read(10,*)
    read(10,*) (Temp(J),J=1,n)

    Flag=0
    do while (Flag==0)
      read(10,30) (Label(J),J=1,5)
      if ((Label(1)=='S').and.(Label(5)=='n')) then
        Flag = 1
      end if
    end do
    read(10,*)
    read(10,*)
    read(10,*) (Sali(J),J=1,m*n)

    extr_sali(1)=3.2
    extr_sali(2)=3.2
    do i=1,m*n
      if (extr_sali(1)>Sali(i)) then
```

```
            extr_sali(1)=Sali(i)
          end if
          if (extr_sali(2)<Sali(i)) then
            extr_sali(2)=Sali(i)
          end if
        end do

        Flag = 0
        do while (Flag==0)
          read(10,30) (Label(J),J=1,5)
          if ((Label(1)=='B').and.(Label(4)=='k')) then
            Flag = 1
          end if
        end do
        read(10,*)
        read(10,*)
        read(10,*) (Entha(J),J=1,n)

        write(13,15) Rho(1:n)
        write(14,15) Rho(n+1:2*n)
        write(15,50) Entha(1:n)
        write(18,15) Temp(1:n)
        write(19,40) Sali(1:n)
        write(20,40) extr_sali(1:2)
        Counter=Counter+1
      end if
    goto 9997
    9998 continue

    1000  read(11,11,end=9999) (Label(J),J=1,5)
       if ((Label(1)=='P').and.(Label(5)=='t')) then
        backspace(10)
        read(11,20) Times(Counter)
        Flag = 0
        do while (Flag==0)
          read(11,36) c1
          if ((c1(6:6)=='Z').and.(c1(18:18)=='L')) then
            Flag = 1
           end if
        end do
        read(11,*)
        read(11,*)
        read(11,*)  VelverL(1:n)

        Flag = 0
        do while (Flag==0)
```

```
      read(11,36) c1
      if ((c1(6:6)=='Z').and.(c1(18:18)=='V')) then
        Flag = 1
      end if
    end do
    read(11,*)
    read(11,*)
    read(11,*) (VelverV(J),J=1,n)

    write(16,50) (VelverL(J),J=1,n)
    write(17,50) (VelverV(J),J=1,n )
    Counter=Counter+1
  end if
  goto 1000
9999  continue


close(10)
close(11)
close(12)
close(13)
close(14)
close(15)
close(16)
close(17)
close(18)
close(19)
close(20)
end
```

Another FORTRAN program is used to identify the high temperature vents at the surface. It tracks the center of the temperature plume at the seafloor, and records the vent fluid temperature and corresponding salinity, although the center of the plume swings with time.

```
program MultiVentSurfSample

implicit none
real :: Times(1000),TempRow(200),SaliRow(200),inTime(10)
integer :: Pos(10),inPos(10),live(10),vent(30)
character :: Label(5), string
integer :: i,k,max,m,n,J,EOF,Counter,Counterm,Flag,vma,T_plume
```

```
write(*,*) 'Input Number of columns'
read(*,*) n

open(unit=10,file='OutFile1',status='old')
open(unit=11,file='Times.dat')

T_plume=250  !the minimum temperature to define a plume
m=10         !maximum number of plumes
vma=2;       !plume is hotter than 2 nodes on both sides

do i=0,m-1
  write(unit=string, fmt='(I1)')  i
  open(unit=12+i,file='Mlvent'//string//'SurfST.dat')
end do

do i=1,m     !the state of the plume node when and whether
  Pos(i)=-3
  inPos(i)=-3
  inTime(i)=-3
end do

Counterm = 1    !pick time and temperature, salinity data
EOF = 0
do while (EOF==0)
  read(10,10,IOSTAT=EOF) (Label(J),J=1,5)
  10 format(5A)

  if ((Label(1)=='P').and.(Label(5)=='t')) then
    backspace(10)
    read(10,20) Times(Counterm)
    20 format(T27,E20.15)
    write(11,*) Times(Counterm)
    Flag = 0
    do while (Flag==0)
      read(10,30) (Label(J),J=1,5)
      30 format(T6,5A)
      if ((Label(1)=='T').and.(Label(5)=='e')) then
        Flag = 1
      end if
    end do
    read(10,*)
    read(10,*)
    read(10,*) (TempRow(J),J=1,200)

    Flag = 0
    do while (Flag==0)
```

```
        read(10,30) (Label(J),J=1,5)
        if ((Label(1)=='S').and.(Label(5)=='n')) then
          Flag = 1
        end if
      end do
      read(10,*)
      read(10,*)
      read(10,*) (SaliRow(J),J=1,200)


      do i=1,m       !pick all the plume at that time slice
        vent(i)=-7
      end do
      Counter=1

if(TempRow(1)>=TempRow(2).and.TempRow(1)>=TempRow(3).and.TempRow(1)>T_plume)
then
        vent(Counter)=1
        Counter=Counter+1
      end if

if(TempRow(2)>TempRow(1).and.TempRow(2)>=TempRow(3).and.TempRow(2)>=TempRow
(4).and.TempRow(2)>T_plume) then
        vent(Counter)=2
        Counter=Counter+1
      end if
      do i=3,n-2
        if (TempRow(i)>TempRow(i-1).and.TempRow(i)>TempRow(i-
2).and.TempRow(i)>=TempRow(i+1)&
        .and.TempRow(i)>=TempRow(i+2).and.TempRow(i)>T_plume) then
        vent(Counter)=i
        Counter=Counter+1
        end if
      end do
      if(TempRow(n-1)>TempRow(n-2).and.TempRow(n-1)>TempRow(n-3).and.TempRow(n-
1)>=TempRow(n).and.TempRow(i)>T_plume) then
        vent(Counter)=n-1
        Counter=Counter+1
      end if
      if(TempRow(n)>TempRow(n-1).and.TempRow(n)>TempRow(n-
2).and.TempRow(i)>T_plume) then
        vent(Counter)=n
        Counter=Counter+1
      end if
      Counter=Counter-1
      if (Counter>10) then
```

```
        write(*,*) 'more than 10 vents', Counter-1
      end if


      do i=1,m        !track plume position in different time, allow plume to move around 2 nodes at
most each time step
        live(i)=-1
        do j=1,10
        if (vent(j)-Pos(i)>-3.and.vent(j)-Pos(i)<3) then
          Pos(i)=vent(j)
          live(i)=1
          vent(j)=-7
          exit
        end if
        end do
      end do

    do i=1,m
       do j=1,10
       if (Pos(i)<0.and.vent(j)>0) then
          Pos(i)=vent(j)
          live(i)=1
          inPos(i)=vent(j)    !where and when the plume starts
          inTime(i)=Counterm
          vent(j)=-7
       end if
       end do
    end do

   Counter=0    !report a message to screen if there are too many vents to be tracked including
old vents
   do i=1,m
      if (vent(i)>0) then
          write(*,*) vent(i)
          Counter=Counter+1
      end if
   end do

   if (Counter>0) then
     write(*,*) 'too many vents', Counter
   end if

    do i=1,m
     if (Pos(i) >= 0) then
       write(11+i,*) Times(Counterm),TempRow(Pos(i)),SaliRow(Pos(i)),Pos(i),live(i)
     end if
```

```
    end do
   Counterm = Counterm+1
   end if
end do

max = inTime(1)
do i=1,m
  if (max < inTime(i)) then
    max = inTime(i)
  end if
end do


  if (max > 1) then  !add early information for the vent accessing to the surface late, inTime is
when the plume accessing to the surface
    Counterm = 1
    rewind(10)
    EOF=0
    do while (EOF==0)
       read(10,10,IOSTAT=EOF) (Label(J),J=1,5)
       if ((Label(1)=='P').and.(Label(5)=='t')) then
          backspace(10)
          read(10,20) Times(Counterm)
          Flag = 0
          do while (Flag==0)
             read(10,30) (Label(J),J=1,5)
             if ((Label(1)=='T').and.(Label(5)=='e')) then
                Flag = 1
             end if
          end do

          read(10,*)
          read(10,*)
          read(10,*) (TempRow(J),J=1,200)

          Flag = 0
          do while (Flag==0)
             read(10,30) (Label(J),J=1,5)
             if ((Label(1)=='S').and.(Label(5)=='n')) then
                Flag = 1
             end if
          end do
          read(10,*)
          read(10,*)
          read(10,*) (SaliRow(J),J=1,200)
          do i=1,m
```

```
            live(i)=-1
            if (inTime(i) > Counterm) then
               write(11+i,*)
Times(Counterm),TempRow(inPos(i)),SaliRow(inPos(i)),inPos(i),live(i)
            end if
          end do
        Counterm=Counterm+1
        end if
        if (Counterm==max) then
           exit
        end if
      end do
  end if

do i=1,m+2
  close(9+i)
end do

end
```

The program below is a FORTRAN code recording vent fluid temperature and salinity at different time slices at a given user-defined position at the seafloor.

```
program VentSurfSample !track maximum temperature and correspoing salinity at different time
slice

implicit none
real :: SurfTemps(1000),SurfSals(1000), &
     Times(1000),TempRow(200),SaliRow(200)
integer :: Pos(3)
character :: Label(5)
integer :: i,k,n,J,EOF,Counter,Flag

open(unit=10,file='OutFile1',status='old')
open(unit=11,file='Times.dat')
open(unit=12,file='SurfventTemps.dat')
open(unit=13,file='SurfventSals.dat')

write(*,*) 'Input Number of columns'
read(*,*) n

Counter = 1            !pick out time, temperature and salinity
```

```
EOF = 0
do while (EOF==0)
  read(10,10,IOSTAT=EOF) (Label(J),J=1,5)
  10 format(5A)
  if ((Label(1)=='P').and.(Label(5)=='t')) then
    backspace(10)
    read(10,20) Times(Counter)
    20 format(T27,E20.15)
    write(11,*) Times(Counter)
    Flag = 0
    do while (Flag==0)
      read(10,30) (Label(J),J=1,5)
      30 format(T6,5A)
      if ((Label(1)=='T').and.(Label(5)=='e')) then
        Flag = 1
      end if
    end do
    read(10,*)
    read(10,*)
    read(10,*) (TempRow(J),J=1,200)

    Flag = 0
    do while (Flag==0)
      read(10,30) (Label(J),J=1,5)
      if ((Label(1)=='S').and.(Label(5)=='n')) then
        Flag = 1
      end if
    end do
    read(10,*)
    read(10,*)
    read(10,*) (SaliRow(J),J=1,200)

    SurfTemps(Counter) = TempRow(1)
    do i=1,n
      if(SurfTemps(Counter)<TempRow(i)) then
        SurfTemps(Counter)=TempRow(i)
      end if
    end do
    k=1
    Pos(1)=-1
    Pos(2)=-1
    Pos(3)=-1
    do i=1,n
      if(SurfTemps(Counter) == TempRow(i)) then
      Pos(k)=i
      k=k+1
```

```
      end if
    end do
    SurfSals(Counter)=SaliRow(Pos(1))
    write(12,*) SurfTemps(Counter),Pos(1),Pos(2),Pos(3)
    write(13,*) SurfSals(Counter), Pos(1)
    Counter=Counter+1
  end if
end do

close(10)
close(11)
close(12)
close(13)
end
```

The matlab code as below is to calculate the heat flux from the output of program 'HeatSaltflux' mentioned above, assuming vertical mass flux from the node at the second row to the node at the first row equals to mass flux at that position at the seafloor.

```
%%%%Calculate heatflux Assuming mass flux from second row = mass flux at
%%%%the surface (middle of first row)

load('Density2.dat')
load('Enthalpy.dat')
load('Times.dat')
load('VelVL.dat')
load('VelVV.dat')
%load('SurfHeatFlux.dat')

w=25;%width of node
Heatf_bound1=150;%150MW/km is the minimum value to consider the hydrothermal vents
active
bound_percent=0.70;
Vel=VelVL+VelVV;

[m,n]=size(Vel); %only consider upflow for heat flux
for i=1:m
   for j=1:n
      if Vel(i,j)>0
         Vel(i,j)=0;
      else
```

```
            Vel(i,j)=-Vel(i,j);
        end
    end
end

for i=1:m
    Heatf(i,1)= (Enthalpy(i,1)-Enthalpy(i,n))*Density2(i,1)*Vel(i,1)*w/2;
    for j=2:n-1
        Heatf(i,j)= (Enthalpy(i,j)-Enthalpy(i,n))*Density2(i,j)*Vel(i,j)*w;
    end
    Heatf(i,n)=0;
end

for i=1:m
    Hf(i,1)=sum(Heatf(i,:));
end

Hf=2*Hf/1000; %consider full space, and change unit from w/m to Mw/km

m1=floor((1-bound_percent)*m);  %low cut the beginning time series which smaller than bound
value based on bound percent to make an average
Heatf_bound=mean(Hf(m1:m,1));
start=m;

for i=1:m
    if Hf(i,1)>Heatf_bound
        start=min(i,start);
    end
end

Heatf_aver=mean(Hf(start:m,1));

plot(Times,Hf);
hold on;
Y=[0,100],Z=[Heatf_aver,Heatf_aver];
plot(Y,Z);
hold on;
```

APPENDIX B: FINER SCALE SIMULATION

In order to study whether node size of the numerical model affects the simulation result significantly, the simulation S6 in Table 3.1 was rerun using 10 m by 10 m node size instead of 25 m by 25 m. The finer scale simulation is denoted S6*.

As shown in Figure B.1 and B.2, finer scale (10m by 10m) simulation produces clearer plumes, and depicts the plume splitting to the bottom of the system, but it does not change either the thermal structure or vent fluid temperature and salinity evolution much. We also compare a few main features of the two models in Table B.1. Compared to the simulation S6, the simulation S6* produces ~10 °C higher vent fluid temperature, and vent fluid salinity is closer to that of seawater, but generally the main features are very similar.

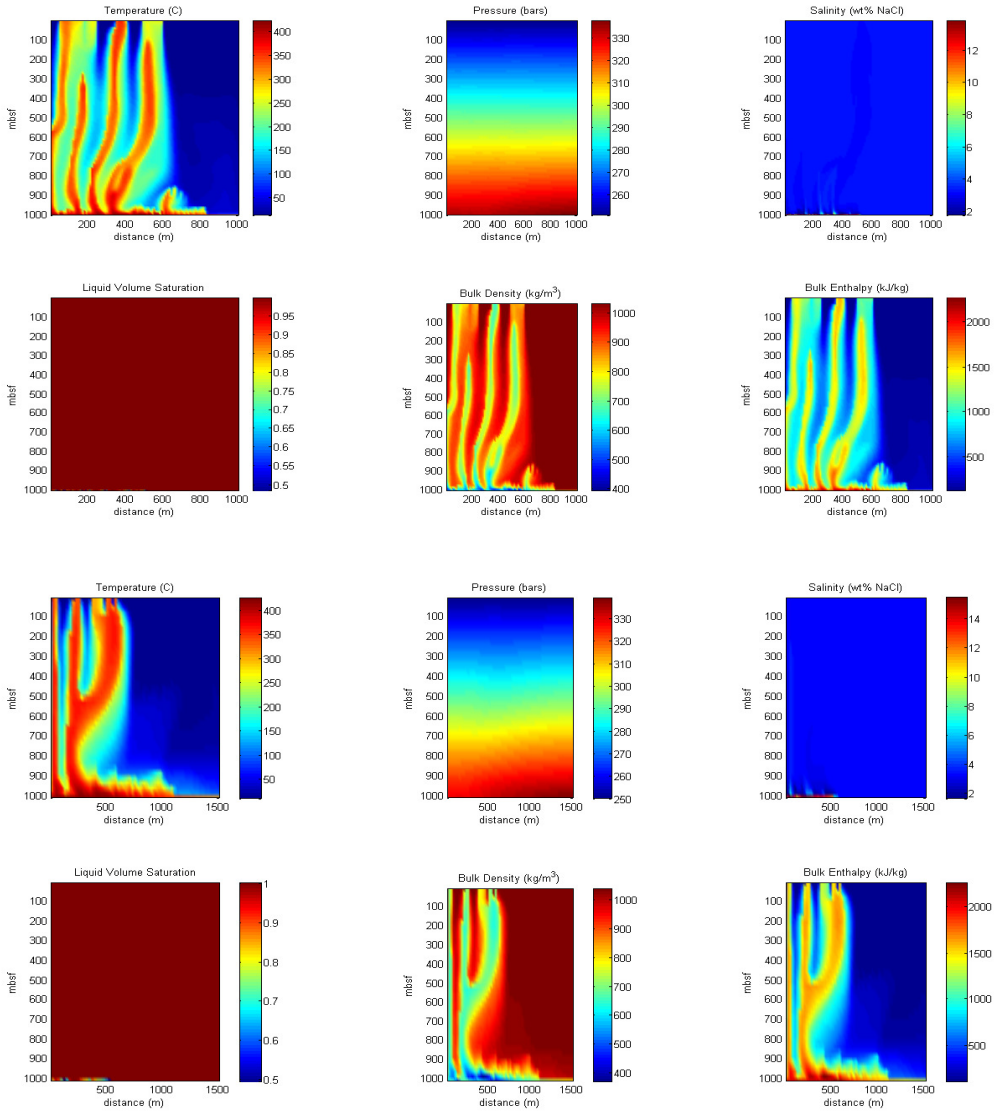

Figure B.1 Comparison of the plume structures of simulation S6* and S6 using different node size. The plot of simulation S6* at the top uses 10 m by 10 m node size, while that of simulation S6 at the bottom uses 25 m by 25 m, which is presented in chapter 3. Both simulations are at year ~8. Note that the horizontal distance of the finer scale simulation is 1km instead of 1.5 km.

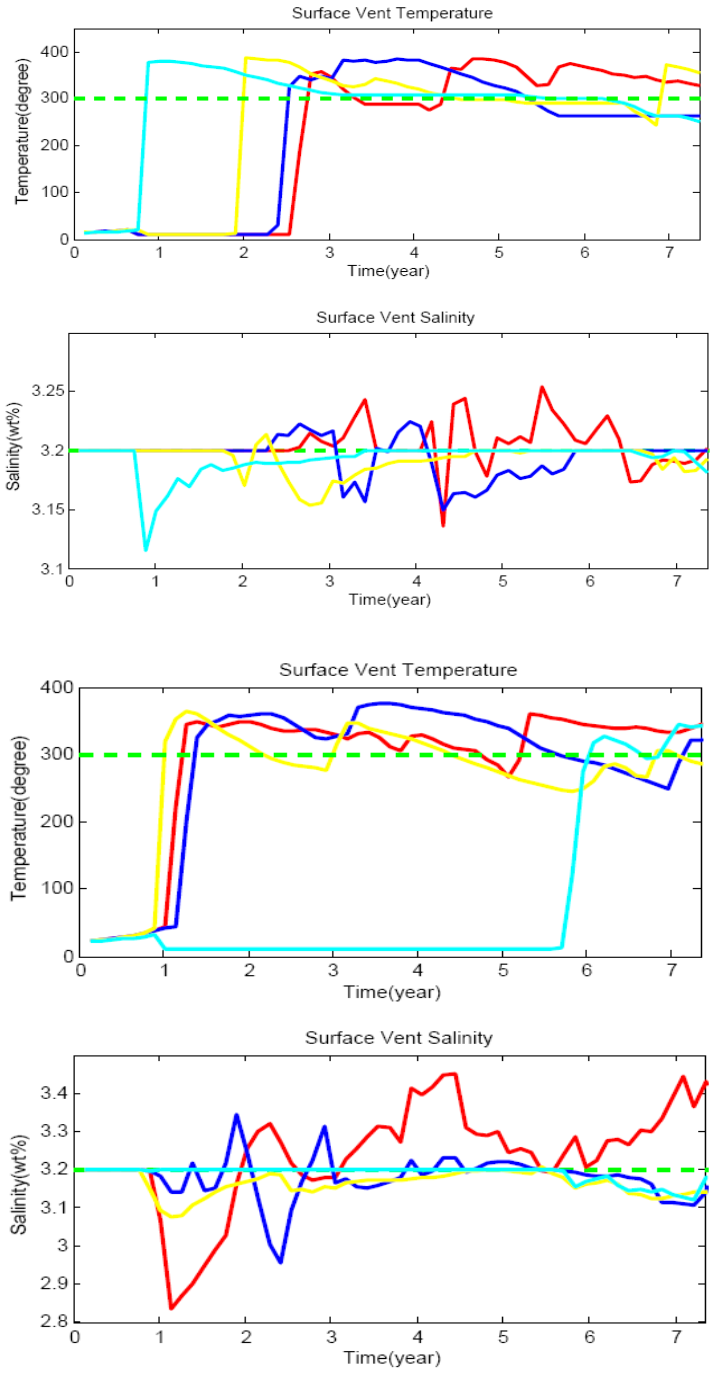

Figure B.2 Comparison of vent fluid temperature and salinity evolution of simulation S6* and S6 using different node size. The plot of simulation S6* at the top uses 10 m by 10 m node size, while that of simulation S6 at the bottom uses 25 m by 25 m, which is presented in chapter 3.

Table B.1 Comparison of main features of simulation S6 and S6*

Comparison	S6	S6*
Max vent temperature (°C)	376.0	386.8
Mean vent temperature (°C)	351.6	368.3
Max vent brine salinity (wt%)	3.45	3.31
Mean vent brine salinity (wt%)	3.30	3.23
Max bottom brine salinity (wt%)	15.88	15.87
Mean bottom brine salinity (wt%)	15.38	14.70
Min vent vpor salinity (wt%)	2.83	3.09
Mean vent vapor salinity (wt%)	3.12	3.17
Min bottom vapor salinity (wt%)	1.01	1.02
Mean bottom vapor salinity (wt%)	1.60	1.54
Mean surface heat flux (Mw/km)	229.8	199.5

Heat flux is estimated using the same size of vent field (50 m wide in the off axis direction).

APPENDIX C: ADDITIONAL SIMULATIONS

In addition to the simulations discussed in chapter 3, we have also run additional simulations with system depth of 1.5 km and 2 km, however they have the same surface pressure of 25 MPa and bottom temperature range of 400-500 °C, as shown in Table C.1.

The simulations in Table 3.1 and Table C.1 are used to explore the effect of parameters of MaxTbot and system depth on several features of fluid temperature and salinity. These features include max vent temperature, mean vent temperature, min bottom vapor salinity, mean bottom vapor salinity, max bottom brine salinity, mean bottom brine salinity, min vent VDF salinity, mean vent VDF salinity, max vent BDF salinity, mean vent BDF salinity and heat flux. These features are defined as below.

In the simulations, single or multiple plumes vent at the seafloor after a certain time, the vent fluid temperature and salinity evolution with time plots (for example, Figure 3.4) track the center, which is hottest in the nearby area, of the individual plume at the seafloor in continuous time slices. Note the temperature of the center of the hottest plume as Ti (i is the order of the time slice). The time slices of the beginning part of the simulation when the vent is not hot enough (< 300°C) are not considered. The sampling rate is 8 time slices per year for permeability of 10^{-12} m^2, and 4 time slices per year for permeability of 10^{-13} m^2.

Max vent temperature T_{vmax} is defined as

$$T_{vmax} = \max (Ti) \tag{6}$$

Mean vent temperature T_{vmean} is defined as

$$T_{vmean} = \text{mean} (Ti) \tag{7}$$

Based on phase diagram (Figure 3.2), higher MaxTbot will result in greater salinity brine and lower salinity vapor at the top of AMC where phase separation occurs, provided bottom pressure and initial salinity are the same. If fluid with different salinity from normal seawater due to phase separation exists at the top of AMC in a certain time slice i (i is the order the time slice), note the minimum fluid salinity (vapor) as S_{bvi}, and the maximum fluid salinity (brine) as S_{bbi}. They are both very stable except in the beginning part of the evolution. For example, after the first 5 years for the system with permeability of 10^{-13} m^2, the maximum brine salinity varies by ~1.5 wt% and the minimum vapor salinity varies by ~0.5 wt%. So the beginning part of the evolution is not considered.

Min bottom vapor salinity S_{bvmin} is defined as

$$S_{bvmin} = \min (S_{bvi}) \tag{8}$$

Mean bottom vapor salinity S_{bvmean} is defined as

$$S_{bvmean} = \text{mean} (S_{bvi}) \tag{9}$$

Max bottom brine salinity S_{bbmax} is defined as

$$S_{bbmax} = \text{Max}(S_{bbi}) \tag{10}$$

Mean bottom brine salinity S_{bbmean} is defined as

$$S_{bbmean} = \text{mean} (S_{bbi}) \tag{11}$$

Similarly, note the lowest vapor salinity (< 3.2 wt%) at the surface at a certain time slice as vent VDF salinity S_{vvi}, and the highest BDF salinity (> 3.2 wt%) as vent brine salinity S_{vbi} (i is the order of the time slice). Because VDF and BDF could vent at the seafloor simultaneously, both VDF and BDF salinity are considered at the same time. If S_{vvi} or S_{vbi} is very close to that of seawater (3.15-3.25 wt%) at a certain time slice, it will not be considered because vent fluid in that phase is not active enough at that time.

Min vent VDF salinity S_{vvmin} is defined as

$$S_{vvmin} = \min (S_{vvi}) \quad (12)$$

Mean vent VDF salinity S_{vvmean} is defined as

$$S_{vvmean} = \text{mean} (S_{vvi}) \quad (13)$$

Max vent BDF salinity S_{vbmax} is defined as

$$S_{vbmax} = \text{Max}(S_{vbi}) \quad (14)$$

Mean vent BDF salinity S_{bmean} is defined as

$$S_{vbmean} = \text{mean} (S_{vbi}) \quad (15)$$

For each time slice, a separate heat flux hf_i (i is the order of time slice) was calculated using the equation and the assumption in Chapter 3. Heat flux changes with time, consistent with vent fluid temperature fluctuating at the vent. Similar to vent fluid temperature, hf_i is pretty low in the beginning of the evolution because the vent at the seafloor is not active yet. Those time slices are not considered in the heat flux calculation.

Heat flux of the system H is calculated by

$$H = \text{mean} (hf_i) \quad (16)$$

All these features of the simulations from Table 3.1 and Table C.1 are plotted in Figures C.1-C.6 as below. In general, several correlations are presented in the plots. Permeability has little effect on the features of fluid temperature and salinity, but it changes heat flux dramatically. Vent fluid temperature and heat flux increases with increasing MaxTbot. As MaxTbot increases, vent VDF salinity and bottom vapor salinity decrease, while vent BDF salinity and bottom brine salinity increase. As system depth increases, vent VDF salinity and bottom fluid vapor salinity increase, while vent BDF salinity and bottom fluid brine salinity decrease. However, due to the

complexity of hot and deep hydrothermal system and limited resolution of our models, further study is required to illustrate those correlations more clearly.

Table C.1 Model setup of the additional simulations.

simulation	MaxTbot (°C)	Depth (km)	Permeability (m^2) (-lg)
1	425	1.5	13
2	450	1.5	13
3	475	1.5	13
4	500	1.5	13
5	425	2	13
6	440	2	13
7	450	2	13
8	475	2	13
9	500	2	13
10	425	1.5	12
11	450	1.5	12
12	475	1.5	12
13	500	1.5	12
14	425	2	12
15	450	2	12
16	475	2	12
17	500	2	12

Values for used constants in FISHES are the same as those in Table 3.1. Seafloor pressure is 250bar.

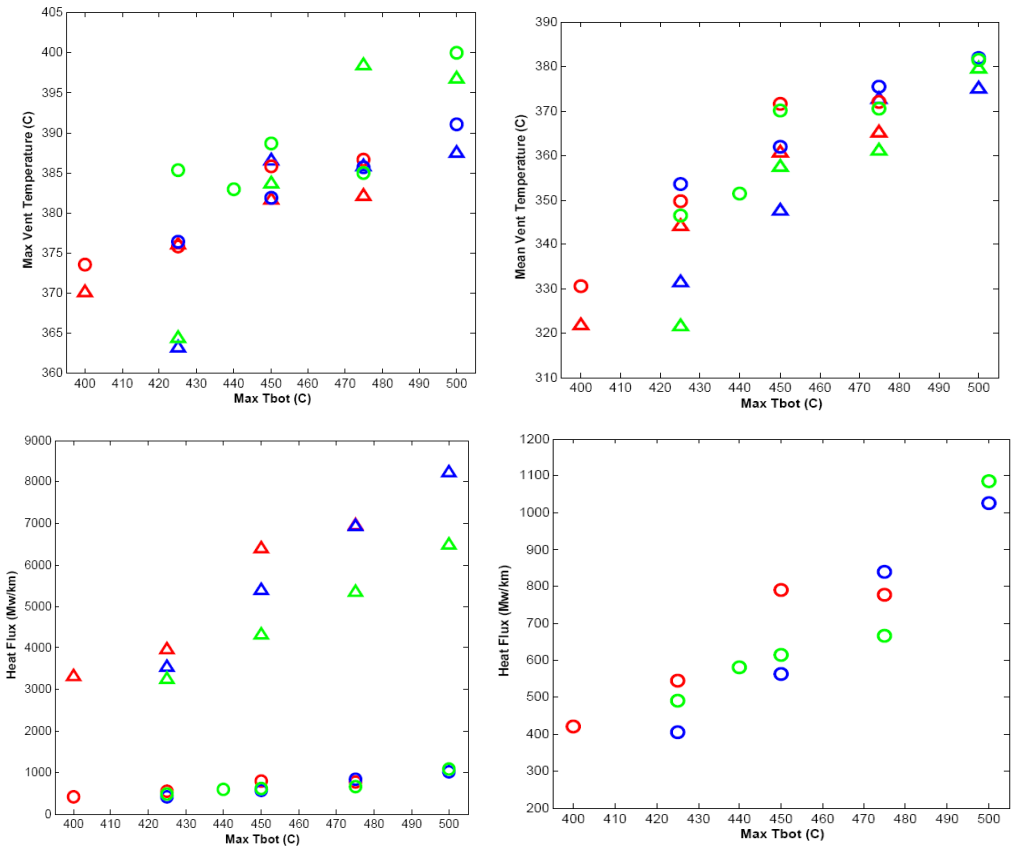

Figure C.1 Vent fluid temperature and heat flux of hydrothermal systems as a function of MaxTbot at a seafloor pressure of 25 MPa. Color shows different system depth; red is 1km deep system, blue is 1.5km deep and green is 2km deep. Shape shows different permeability; triangle is 10^{-12} m^2 and circle is 10^{-13} m^2. Sampling rate is 8/year for permeability of 10^{-12} m^2, 4/year for permeability of 10^{-13} m^2. A general linearly increasing trend is clear in the plot.

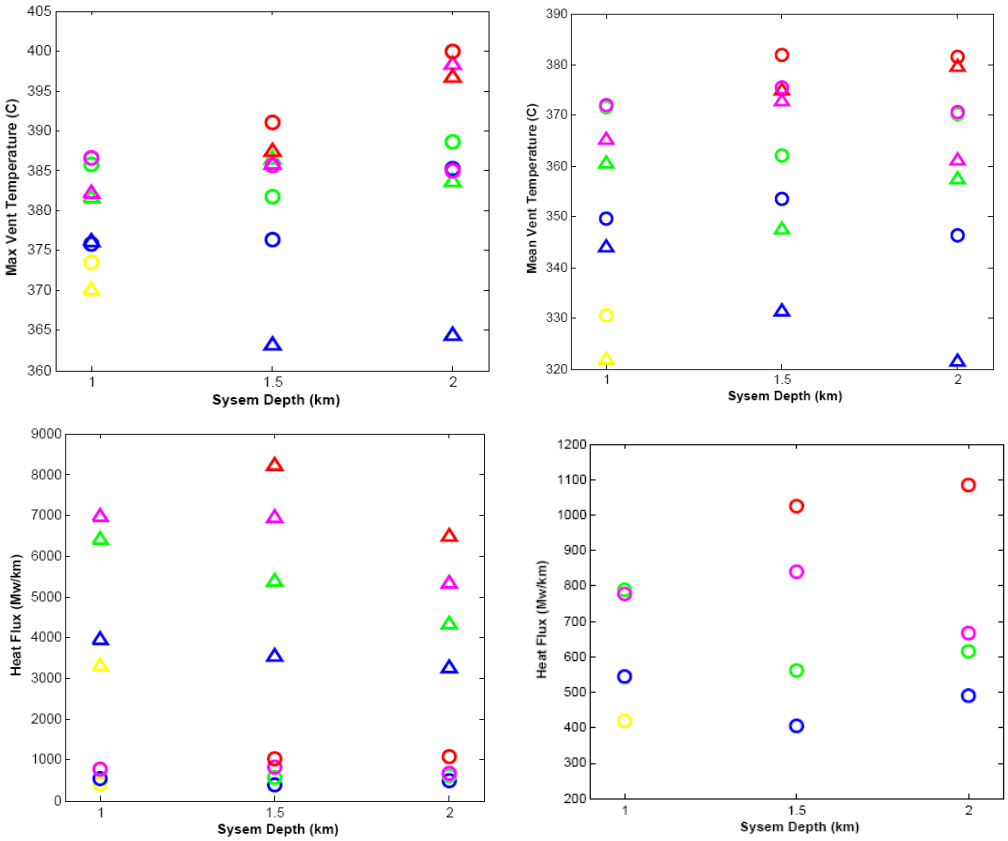

Figure C.2 Vent fluid temperature and heat flux of hydrothermal systems as a function of system depth at a seafloor pressure of 25 MPa. Color shows different max bottom temperature; red is 500 °C, purple is 475 °C, green is 450 °C, blue is 425 °C and yellow is 400 °C. Shape shows different permeability; triangle is 10^{-12} m^2 and circle is 10^{-13} m^2. Sampling rate is 8/year for permeability of 10^{-12} m^2, 4/year for permeability of 10^{-13} m^2. No strong correlation is observed except that heat flux of the system with permeability of 10^{-12} m^2 slightly decreases with increasing system depth.

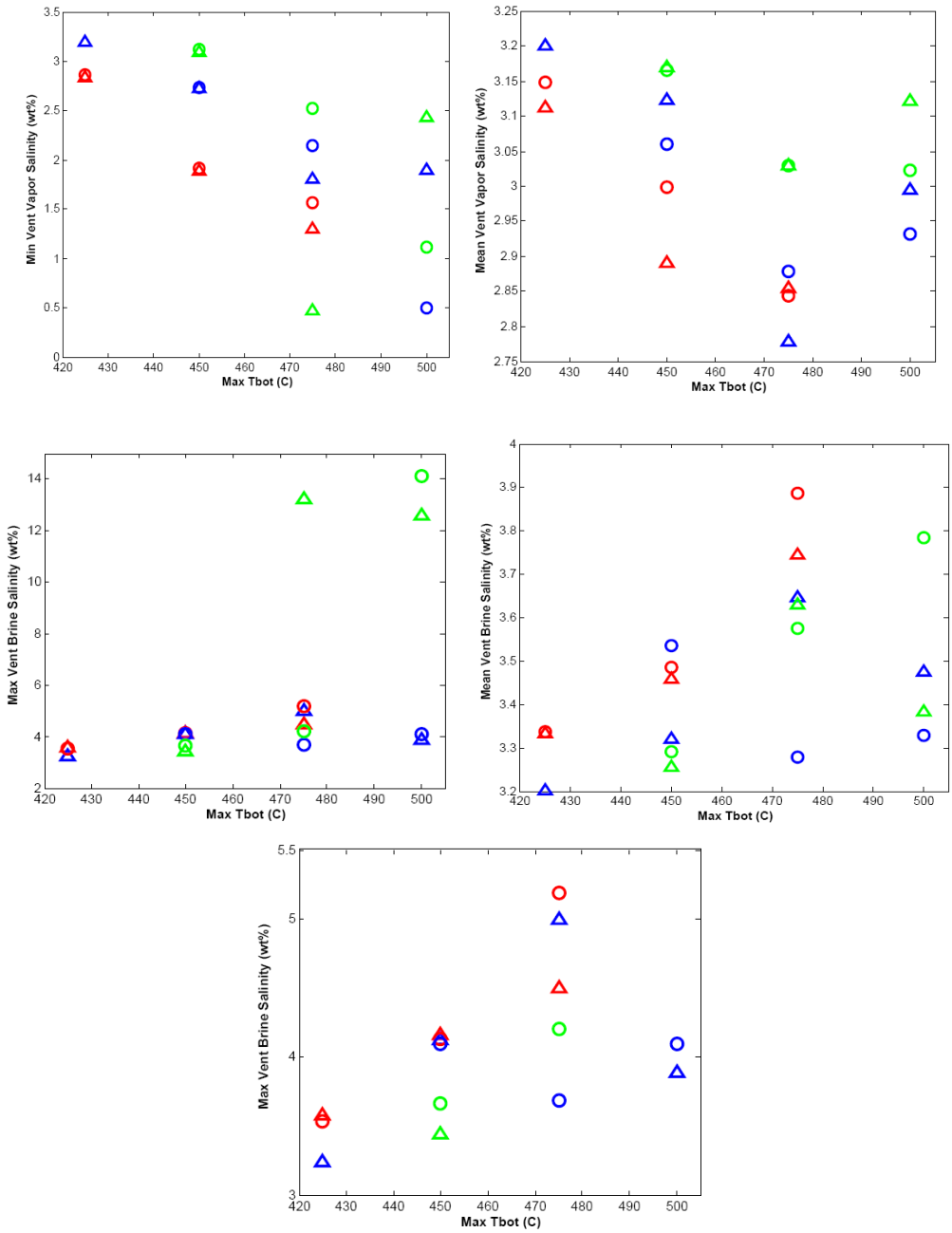

Figure C.3 Vent VDF and BDF salinity of hydrothermal systems vs MaxTbot at a seafloor pressure of 25 MPa. Color shows different system depth; red is 1km deep system, blue is 1.5km deep and green is 2km deep. Shape shows different permeability; triangle is 10^{-12} m^2 and circle is 10^{-13} m^2. Sampling rate is 8/year for permeability of 10^{-12} m^2, 4/year for permeability of 10^{-13} m^2. VDF salinity generally decreases with increasing bottom temperature, while BDF salinity increases with increasing bottom temperature. The permeability generally doesn't change vent VDF or BDF salinity except in the hot or deep system. The last figure is a plot of the third one in different scale.

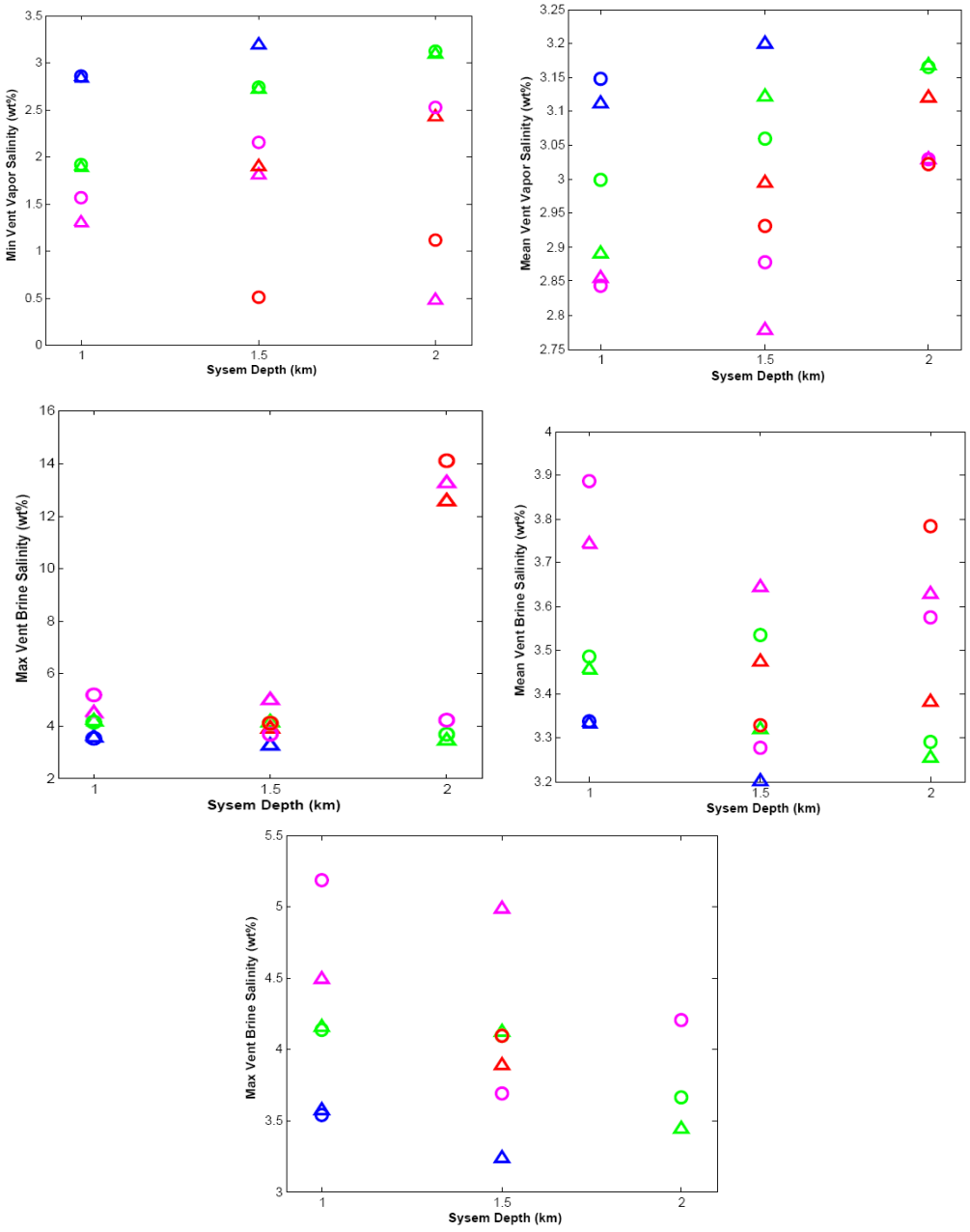

Figure C.4 Vent VDF and BDF salinity of hydrothermal systems as a function of system depth at a seafloor pressure of 25 MPa. Color shows different max bottom temperature; red is 500 °C, purple is 475 °C, green is 450 °C, blue is 425 °C. Shape shows different permeability; triangle is 10^{-12} m^2 and circle is 10^{-13} m^2. Sampling rate is 8/year for permeability of 10^{-12} m^2, 4/year for permeability of 10^{-13} m^2. VDF salinity generally increases with increasing system depth, while BDF salinity decreases with increasing system depth. The last figure is a plot of the third one in different scale.

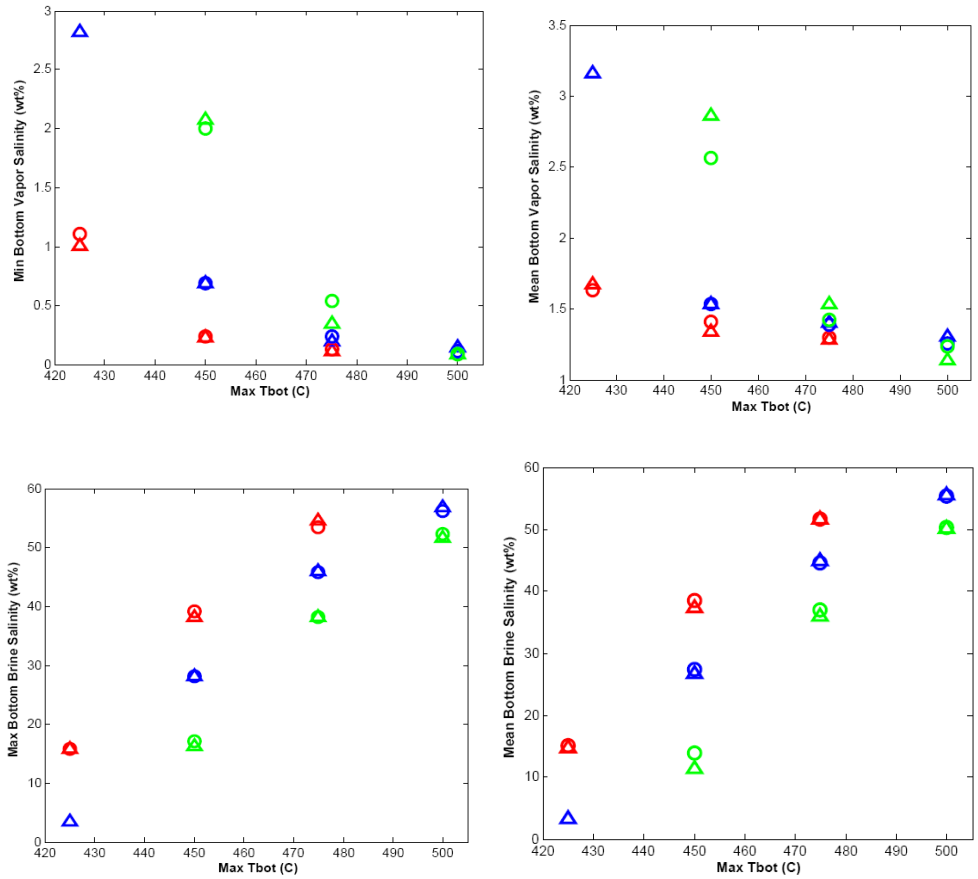

Figure C.5 Bottom vapor and brine salinity of hydrothermal systems vs MaxTbot at a seafloor pressure of 25 MPa. Color shows different system depth; red is 1km deep system, blue is 1.5km deep and green is 2km deep. Shape shows different permeability; triangle is 10^{-12} m^2 and circle is 10^{-13} m^2. Sampling rate is 8/year for permeability of 10^{-12} m^2, 4/year for permeability of 10^{-13} m^2. Vapor salinity generally decreases with increasing bottom temperature, while brine salinity increases with increasing bottom temperature. The permeability doesn't make change to bottom vapor or brine salinity.

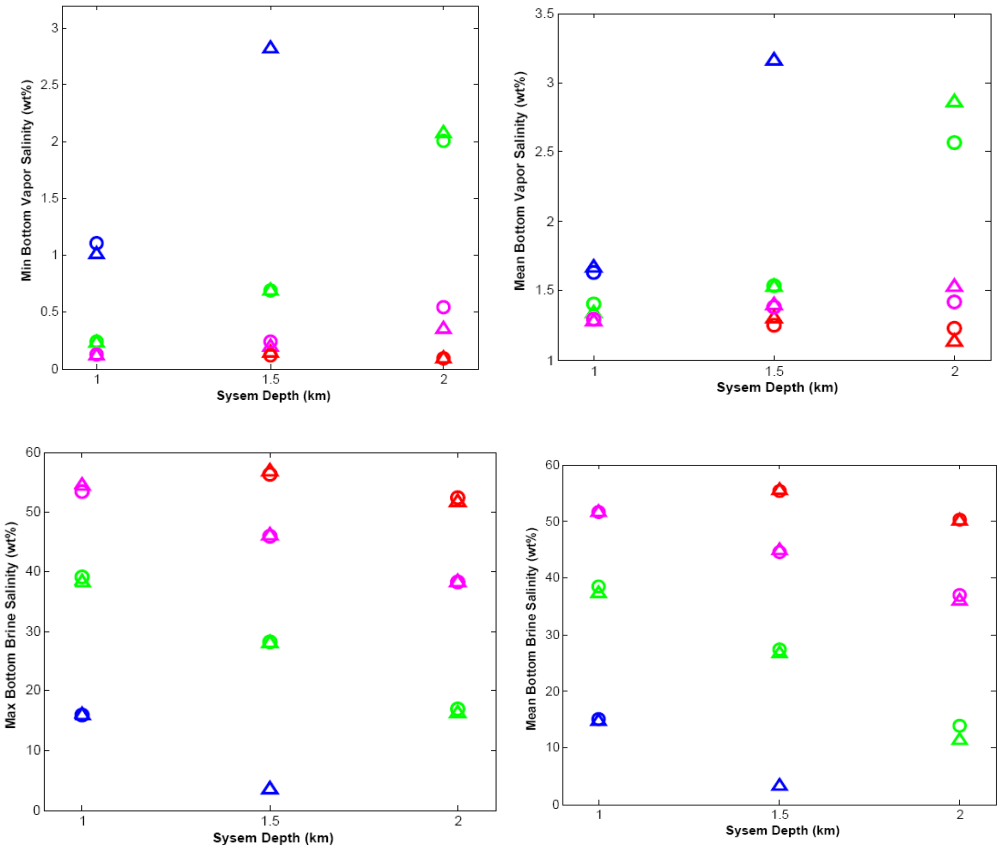

Figure C.6 Bottom vapor and brine salinity of hydrothermal systems as a function of system depth at a seafloor pressure of 25 MPa. Color shows different max bottom temperature; red is 500 °C, purple is 475 °C, green is 450 °C, blue is 425 °C. Shape shows different permeability; triangle is 10^{-12} m^2 and circle is 10^{-13} m^2. Sampling rate is 8/year for permeability of 10^{-12} m^2, 4/year for permeability of 10^{-13} m^2. Vapor salinity increases with increasing system depth, while brine salinity decreases with increasing system depth.